JNK signaling in pioneer neurons directs the architectural organization of the CNS and coordinates the motor activity of the *Drosophila* embryo

Katerina Karkali[1,2,4], Timothy E. Saunders[2], Samuel W. Vernon[3], Richard A. Baines[3], George Panayotou[4] and Enrique Martín-Blanco[1,2] *

1. Instituto de Biología Molecular de Barcelona (CSIC), Parc Cientific de Barcelona, Baldiri Reixac 10-12, 08028 Barcelona, Spain

2. Mechanobiology Institute and Department of Biological Sciences, 5 Engineering Drive 1, National University of Singapore, 117411 Singapore

3. Division of Neuroscience and Experimental Psychology, School of Biological Sciences, Faculty of Biology, Medicine and Health, University of Manchester, Manchester Academic Health Science Centre, Manchester, M13 9PL, UK.

4. BSRC Alexander Fleming, 34 Fleming Street, 16672 Vari, Greece

* Correspondence to: embbmc@ibmb.csic.es

ABSTRACT

The Central Nervous System (CNS) organogenesis is a complex process that obeys precise architectural rules. Yet, both the mechanisms dictating CNS structural organization, and the impact that this may have on its functionality remain unknown. Analyzing the Drosophila embryo Ventral Nerve Cord (VNC) morphogenesis, we found that tight control of JNK signaling levels is essential for its stereotyped architectural organization. The JNK pathway is active in a specific subset of pioneer neurons, where it, autonomously, regulates the expression of cell adhesion molecules, the integrity of axons and dendrites, and motoneurons electrophysiological properties. Interfering during early embryogenesis in the activity of JNK signaling in these cells, it affects their pioneer functions and leads to cumulative scaffolding defects during the establishment of axonal networks. This global architectural disarray associates to the failure of the VNC condensation and the coordination of the embryonic motor activities required for hatching. Altogether, our data point to the JNK cascade in a subset of pioneer neurons as a key element underpinning VNC architecture, and reveal critical links between the structural organization of the VNC and its functional optimization.

INTRODUCTION

The complex nervous system of bilaterians is thought to have emerged from an ancient, diffuse nerve plexus [1], which evolved into a stereotyped segmented polarized structure [2]. Within this framework, functional neural circuits [3] [4] [5] arise as precise 3D arrangements of neurons and glial cells [6]. Several lines of evidence suggest a direct relationship between the 3D architectural organization of the nervous system and its functions. First, the spatial distribution of functional circuits in the cortex of vertebrates extensively overlaps with large-scale microstructure, connectivity, and gene expression patterns [7]. Second, in pursuit of functional efficiency, neural networks likely minimize their structural cost following the wiring optimization principle postulated by Ramón y Cajal [8]. These costs may arise from metabolic requirements, signal delay and attenuation, and complex guidance processes [9] and would increase with interneuronal distance [10]. Lastly, the spatial organization of cortical areas appears subject to evolutionary selection [11].

The nervous system's architecture is the outcome of neuro-glial interactions and axon guidance decisions. Yet, how the nervous system achieves a mechanically balanced organization throughout morphogenesis, while neuronal connectivity is being established, is poorly understood. We postulate; first, that coordinated cell communication events must be triggered to direct the acquisition of a specific 3D neural architecture; and second, that accuracy in nervous system spatial organization/topography is essential for its functionality.

To explore these hypotheses, we made use of the developing *Drosophila* embryo Central Nervous System (CNS), in particular the Ventral Nerve Cord (VNC). The mature VNC is composed of segmentally iterated ganglia with a stereotyped pattern of neurons organized in a 3D array. Neurons are surrounded by a cellular meshwork composed of different types of glia and are linked by cohesive axon bundles that establish longitudinal connectives and transverse commissures along the neuropile [12]. The neuronal cell bodies in the VNC are restricted to the cortex, while sensory axons and interneuron projections mostly accumulate in central domains. The positions of neurons and their projections have been mapped by employing segmentally repeated reference points [13]. As embryonic development proceeds, axonal and dendritic arborizations become more complex and, as a whole, the VNC condenses along the anterior-posterior (AP) axis. During condensation, embryos develop sporadic muscle contractions that initially do not correlate with

any sensory input [14] [15]. Yet, over time, these contractions evolve into peristaltic patterns, dependent on coordinated motor circuitry activation, that allow larval hatching [16].

Here, we uncover essential functions for the JNK pathway in a subset of pioneer neurons orchestrating the structural pattern and condensation of the VNC and enabling motor coordination. We find that early in embryogenesis, JNK signaling modulates pioneering events, ensuring the topographical arrangement and fasciculation of axons, and regulates cell adhesion molecules expression. On these bases, JNK facilitates VNC condensation and muscle contractions coordination. At late stages, JNK activity fine-tunes cell bodies allocation and dendrites morphology and numbers. Altogether, our data uncovers a fundamental contribution from the JNK signaling pathway in pioneer neurons to implement CNS architectural organization and to promote functional optimization.

RESULTS

Modular Architecture of the Ventral Nerve Cord (VNC)

The 3D organization of axonal tracts and neuronal bodies dictates the size and shape of the *Drosophila* embryonic VNC. Yet, the spatial distribution of these elements is irregular and noisy, preventing the dissection of the mechanical processes outlining VNC architecture. To identify robust structural landmarks along the VNC scaffold, we performed axial correlation analyses of Fas 2+ axons (**Figures 1A** and **1B**, see also **Movie S1**). Fas 2 is a neural cell adhesion molecule, which highlights a subset of the longitudinal axonal connectives, and whose loss-of-function leads to defasciculation [17]. Correlations along the AP axis uncovered a single characteristic domain in each segment, with a specific (robust) 3D geometrical organization (structural nodes) (**Figure 1C**). These nodes positioned slightly following each posterior commissure (**Figure S1**). At the nodes, the longitudinal connectives were organized in three compact fasciculated units at precise dorso-ventral (DV) and medio-lateral (ML) coordinates (**Figure 1D**). Between nodes, the distribution of fascicles was not correlated between segments (**Figure 1E**). In a posterior direction, noise increased very fast reaching a maximal randomness (minimal correlation) in a mid-position amongst the posterior and the next anterior commissure. Noise then slowly decreased towards the

following node. Thus, within a segment, the 3D structural organization of the VNC is conserved and polarized along the AP axis (**Figure 1F**).

VNC architecture is modulated by JNK signaling

Although the signaling mechanisms directing axon guidance are well understood [18], those employed to coordinate the structural organization and topography of the nervous system remain unexplored. Topography refers to the degree of spatial relation between cells and the cells their axons project to.

We hypothesize that the JNK cascade, which recently emerged as a conserved regulator for axonal growth and regeneration [19] [20], may play a role in shaping the VNC, in part by mechanically regulating neural cells. To investigate this possibility, we interfered with the pathway modulating the kinase activity of the JNK. In most *Drosophila* tissues, the JNK activity is restrained by a negative feedback loop implemented by the dual-specificity phosphatase Puckered (Puc). *puc* expression depends on the activity of Basket (Bsk), the *Drosophila* homologue of JNK, and Bsk function is inhibited by Puc [21]. Although *puc* expression has been reported in the *Drosophila* embryonic CNS [22], its role, if any, in CNS morphogenesis is unknown.

We found that in puc^{E69} and puc^{B48} loss-of-function alleles [21], the structural organization of the VNC was disturbed. The Fas 2+ longitudinal connectives became highly defasciculated and the intersegmental nerves were unevenly distributed. Axons came together irregularly into medial positions and Fas 2 expression was enriched in cell bodies (**Figure 1G** and **S3** and **Movie S2**). In the absence of *puc*, the level of JNK phosphorylation significantly increased in the VNC, supporting the existence of a negative feedback on JNK activity, mediated by *puc* (**Figure S2**). Excessive JNK activity affected axonal organization in the DV and ML axes, but not along the AP direction (**Figure 1H**). The segmental nodes, although less robust and more widely spaced, were still present (**Figure 1I** and **S3**). The increased internodal distance observed in *puc* mutants was manifested as a failure of VNC condensation (on average 18% in puc^{E69} and 39% in puc^{B48} alleles) (see direct measurements of the VNC length in **Figure S4**). Further, the segmentally iterated AP axial structural polarity detected in wild type embryos was abolished (**Figures 1F**).

In brief, a tight control of JNK signaling appears to be essential for implementing the architectural organization of the VNC and for its condensation. This control is exerted, at least in part, by Puc,

124 which restricts JNK activity and promotes cell viability (**Figure S2**).

125

126 **JNK signaling is dynamically regulated in the VNC**

127 To determine, when and where is the JNK cascade active in the VNC we studied the dynamics of
128 *puc* expression, which is itself an early readout of the pathway [21]. A viable Gal4 line under the
129 control of the puc^{E69} enhancer [23] highlighted a segmentally iterated subset of neurons (**Figures**
130 **2A** and **2B**). An increased number of neurons was also observed at the peripheral nervous system
131 (PNS) but no cross-reaction was observed with glial markers [24] (**Figures 2C** and **2D**). *puc*
132 expression in the VNC initiated in a few neurons at the ventral midline at stage 13 (**Figure 2E** and
133 **Movie S3**) and expanded to a minimum consensus of 19 *puc*+ neurons per hemisegment at
134 embryonic stage 17 (**Figure 2F** and **Movie S4**).

135 Dual staining of puc^{E69} embryos with neuronal markers [Even-skipped (Eve) and Engrailed (En)]
136 enabled identification of most of the *puc*+ cells (**Figure S5**). *puc* labeled the aCC, pCC, RP2, U1-
137 U3 (plus weak/variable expression in U4-U5) and 3 out of the 8 to 10 EL interneurons. Meanwhile,
138 NL1, NL2, and iVUM5 En+ neurons were *puc*+. Morphological and positional criteria further
139 enabled the assignment of five other neurons, AD, ADV, dMP2 and 2 VUM En- motoneurons
140 (**Figures 2G** and **2H**). This pattern of *puc*+ neurons was largely conserved in puc^{B48} (**Figure S6**).

141 In summary, JNK highest activity was detected in VUMs, pCC and possibly dMP2 neurons at the
142 ventral midline from stage 13 and subsequently in diverse inter and motoneurons projecting
143 through the longitudinal connectives and the intersegmental nerves.

144

145 **The level of JNK activity in *puc*+ neurons directs the VNC architectural organization**

146 To rule out the possibility that the aberrant architecture of the VNC of *puc* embryos was a
147 secondary consequence of the general disruption of the embryo anatomy, we restricted the loss or
148 gain of JNK activity to different subsets of *puc*+ neurons.

149 The RN2-Gal4 line is specifically expressed in the aCC, pCC and RP2 neurons (**Figure 3A**).
150 Suppressing JNK activity in RN2+ cells by overexpressing Bsk^{DN}, a dominant negative form of
151 Bsk, resulted in the disorganization of the Fas 2+ connectives (**Figure 3B**). Spatial correlations
152 became noisy and irregular, internodal distances enlarged, and the condensation of the VNC failed.
153 We also overexpressed Hep^{CA}, a constitutively active form of Hemipterous (Hep), the *Drosophila*

154 homologue of the JNK kinase MKK7, to hyperactivate the pathway. This strongly affected the
155 connectives, which retained a juvenile, disorganized appearance, and resulted in internodal
156 distance enlargement (**Figure 3C**).

157 The MzVum-Gal4 line is expressed in a few lateral cells and in the 3 VUM motoneurons (**Figure**
158 **3D**). Bsk^{DN} expression in these cells altered the fasciculation of Fas 2+ connectives (**Figure 3E**),
159 while Hep^{CA} expression led to their disorganization, as shown by the noisier spatial correlation
160 profiles (**Figure 3F**). There was also an increase in the internodal distances.

161 The CQ2-Gal4 line drives the expression of UAS-linked genes in the U1 to U5 motoneurons
162 (**Figure 3G**). Neither the inhibition (**Figure 3H**), nor the hyperactivation of the pathway (**Figure**
163 **3I**) resulted in any major structural defects. The VNC architecture in both cases (e.g. nodes
164 positions and spatial correlations) was similar to WT.

165 Altogether, these data indicate that the final precise architectural organization of the VNC, requires
166 carefully tuned levels of JNK activity in the early-specified aCC, pCC, and RP2 pioneers and in
167 the VUM neurons.

168

169 **JNK signaling in pioneer neurons modulates Fasciclin 2 levels**

170 The role of JNK signaling in the overall 3D organization of the VNC suggests the existence of a
171 mechanism that propagates the response to JNK activity of pioneers and VUM neurons throughout
172 the tissue. While growth factors or neurotransmitters can be an important source of instructive
173 information [25], adhesion molecules themselves (e.g. Fas 2) may also act as key elements for
174 communication in large-scale processes [26] [27] [28] [29]. In this context, we explored whether
175 the global effects of *puc* could be associated with Fas 2 deregulation or subcellular mislocalization.
176 Fas 2 was enriched at the segmental nodes, irrespectively of the genotype (*wt*, and puc^{E69} and
177 puc^{B48} mutant embryos) (**Figures 4A-C**). Yet, at high JNK activity, in the absence of Puc, its level
178 was reduced by 50%, both in nodes and internodes (**Figure 4D**) and overall, in stage 16 embryo
179 extracts (**Figure 4E**). An equivalent decrease was also observed throughout the CNS after
180 hyperactivating JNK in just the RN2+ neurons (**Figure S7**). Importantly, this effect on Fas 2 levels
181 is autonomously restricted to the aCC, pCC and RP2 neurons and differences in expression outside
182 targeted cells were marginal (**Figure S8**). Further, restricting JNK hyperactivation to discrete
183 segments clearly supported autonomous regulation. Employing a parasegment specific PS8/13-

184 Gal80 transgene [30], we silenced the overexpression of Hep^{CA} by the RN2-Gal4 driver in
185 segments A4-A9. These embryos showed reduced Fas 2 expression anteriorly but normal levels in
186 posterior segments (**Figure S9**).

187 To explore the roles of Fas 2 in the architectural organization of the VNC and its condensation, we
188 employed a series of allelic combinations between hypomorphic (*Fas* 2^{E76} and *Fas 2-GFP*^{CB03613})
189 and null (*Fas* 2^{EB112}) alleles. We found consistent, although mild, VNC condensation defects
190 associated to an extensive defasciculation of Fas 2+ longitudinal tracts. Segmental nodes were
191 present but the 3D correlation along the AP axis was less distinct (**Figure 4F-G)** Further, VNC
192 condensation was reduced, with the VNC length increased compared to WT (**Figure 4H**). These
193 defects partially resemble *puc* alleles phenotypes and indicate a role for Fas 2 in the structural
194 refinement of the VNC and its condensation. Yet, they do not support an exclusive role for Fas 2
195 as the single mediator of JNK activity during VNC morphogenesis. Indeed, the rescue of *puc*^{E69}
196 mutant embryos by pan-neural (ELAV-Gal4) overexpression of the full-length Fas 2^{PEST+} isoform
197 [31] fails to suppress VNC structural or condensation defects (**Figure S10**).

198 In summary, Fas 2 is essential for a correct VNC structural organization and condensation but it is
199 not the unique mediator of the JNK pathway. Yet, the cell adhesion landscape of pioneer neurons
200 appears to have a significant role in the relay mechanisms operating downstream of JNK during
201 tissue shape remodeling (see Discussion).

202

203 **JNK signaling influences the axodendritic organization of *puc*-expressing neurons**

204 Besides the contribution on modulating adhesion cues (see above), the global effects of JNK
205 signaling on VNC architecture may be structural. We examined the morphology of *puc*-expressing
206 neurons [RN2 (aCC, pCC and RP2)] upon Hep^{CA} overexpression for defective structural layouts.

207 aCC is a motoneuron whose axon gets incorporated into the intersegmental nerve (ISN)[32]. Its
208 dendritic arbor develops in a distinct region of the ISN myotopic dendritic domain and consists of
209 8 to 10 dendrites[33] of an average length of 4 µm (**Figure 5A**). pCC is a medially-located
210 interneuron whose axon extends ipsilateral in an anterior direction [34]. Finally, RP2 is a
211 motoneuron, whose axon proceeds through the posterior root of the ISN [35] [32] and branches
212 out between 7 and 9 dendrites, with an average length of 4 µm (**Figure 5A**).

213 As a consequence of the overexpression of Hep^{CA} in RN2+ neurons, the cell bodies of the aCC,

214 pCC and RP2 were frequently misplaced and came together towards the midline (compare **Figures**
215 **5A** and **5B**). The appearance of their axons was also affected; they thickened (**Figures 5B**),
216 increased in length (for pCC and RP2) (**Figures 5C**) and developed a wiggly morphology (**Figure**
217 **5D**). JNK hyperactivation also affected the density (**Figure 5E**) and length (**Figure 5F** and **Movie**
218 **S5**) of dendrites. Summarizing, increasing JNK activity in specific pioneer neurons leads to local
219 structural and topographical disarrays that could seed for mistaken 3D arrangements and
220 cumulative misrouting.

221

222 **JNK activity in pioneer neurons is essential for embryonic motor coordination**

223 Considering the roles of JNK signaling on promoting VNC architectural robustness, we
224 investigated their potential functional consequences. To do so, we focused on motor circuits and
225 evaluated late embryonic activity patterns[14, 16] (**Figure 6A** and **6B**) (see Methods, **Figure S11**
226 and **Movie S6**). In wild type conditions, developing embryos execute forward and backward waves
227 of peristalsis by coordinating bilaterally symmetrical muscle contractions [36] [16]. We found that
228 these movements matured through five stages (**Figure 6C**): they began with brief, isolated,
229 unilateral twitches and sporadic head pinching (stage A). This was followed first by a prolonged
230 rest period occasionally interrupted by uncoordinated single contractions (B) and then by an active
231 stage showing frequent incomplete and complete peristalsis (C). Peristalsis then ends with a short
232 resting period (D), which precedes violent head movements and multiple complete peristalsis (E)
233 leading to the rupture of the vitelline membrane and larval hatching (see also **Figure S11** and
234 **Movie S7**).

235 In the complete absence of *puc* (*puc*^{E69}), the progression of motor patterns was interrupted, and
236 embryos remained indefinitely in an immature stage (A) characterized by occasional unilateral
237 twitches and incomplete peristalsis (**Figure 6D**, **Figure S11** and **Movie S8**). Muscle integrity and
238 functionality were not affected. This systemic failure of motor coordination could be a direct
239 consequence of the increase of JNK activity levels in the CNS in *puc* mutants or the outcome of
240 other non-defined non-autonomous events. To discard this last possibility, we overexpressed
241 Hep^{CA} in RN2 (**Figure 6E** and **6F**) or MzVum cells (**Figure 6G** and **6H**). In both cases, an excess
242 of JNK activity in *puc*+ neurons resulted in a phenotype equivalent to that observed in *puc*^{E69}. Only
243 occasional unilateral twitches, head pinches and infrequent incomplete peristalsis were observed.
244 Therefore, the motor defects in *puc* are a direct response to the loss of Puc activity in *puc*+ neurons.

245 The misregulation of the JNK activity in the same neurons appears to be associated to both VNC
246 structural and embryonic motor coordination defects.
247
248 **JNK signaling modulates motoneuron firing but not synaptic vesicle transport**
249 Some *puc*+ cells are motoneurons and at aberrant levels of JNK activity, their signaling capability
250 might be impaired. This might result in defects in the embryo's motor coordination independently
251 of the architectural organization of the VNC.
252 To test this possibility, we first studied the axonal transport of synaptic vesicles (Synaptotagmin)
253 in the intersegmental nerve [aCC and RP2 (RN2-Gal4) and VUM motoneurons (MzVum-Gal4)]
254 (see Methods, **Figure S12** and **Movie S9**). We found that synaptic vesicles in wild type embryos
255 moved at the same speed and had the same lifetime in aCC/RP2 and VUMs axons, although they
256 were at higher density in RN2+ neurons. No differences were observed either between anterograde
257 and retrograde transport. Upon co-expression of Hep^{CA} in RN2 and MzVUM cells, synaptotagmin
258 transport behavior was largely unaffected (**Figure S12)**, indicating that microtubule-mediated
259 transport remained fully functional.
260 To directly address if the JNK activity influences motoneuron function, we undertook patch clamp
261 recordings from the aCC and RP2 motoneurons, which receive identical cholinergic synaptic
262 inputs [37]. Neurons were voltage-clamped at -60mV to record endogenously produced
263 cholinergic synaptic currents [Spontaneously Rhythmic Currents (SRCs)]. We found that
264 expression of Hep^{CA} in RN2 + neurons did not influence SRC amplitude or frequency (**Figure 7A**
265 and **7B**), indicating that the synaptic input to aCC/RP2 remained unaffected. However, current
266 clamp recordings, in which no holding potential was applied (I=0), revealed that the motoneuron
267 Resting Membrane Potential (RMP) was significantly increased and the membrane hyperpolarized
268 (**Figure 7C** and **7D**). Consequently, the average number of action potential fired per Excitatory
269 PostSynaptic Potential (EPSP) was also notably reduced. We conclude that although the synaptic
270 drive was normal upon JNK hyperactivation, excitability, and thus endogenous firing, was
271 considerably reduced in pioneer motoneurons due to a more negative RMP.
272 Summarizing, the JNK signaling pathway affects pioneer neuron morphology and dendrite
273 integrity but does not affect synaptic vesicle transport or neuron sensory competencies. However,
274 it modulates their firing response.

275

276 **Different temporal roles for the JNK pathway**

277 To define if the inputs of the JNK pathway modulating the structural organization and functional
278 optimization of the VNC are causally related or independent, we evaluated the effects of interfering
279 in the JNK activity levels within the VNC at different times.

280 Programmed temperature shifts between 29 and 18ºC or *vice versa* (see Methods) allowed us to
281 selectively overexpress Hep^{CA} early vs late during embryogenesis. The early-only (stage 10-13)
282 hyperactivation of JNK in RN2+ neurons, before the initiation of neural activity [38], was
283 associated with defects on the morphology of dendrites and axons, with axonal scaffold anomalies
284 and with the collapse of RN2+ neurons towards the midline (**Figure 7E**). VNC condensation was
285 also affected (**Figure 7F**). Furthermore, although these embryos occasionally hatched, they
286 displayed strong muscle coordination defects with an almost complete absence of bilateral
287 peristalsis (**Figure 7G** and **Movie S10**). Conversely, the late hyperactivation of the JNK pathway
288 (stage 15-16) did not affect VNC condensation or peristalsis (**Figures 7F** and **7G** and **Movie S10**).
289 However, it resulted in the misalignment of RN2+ neurons, which displayed scarce and long
290 dendrites, and in the formation of heterogeneous axon bundles (**Figure 7E)**.

291 Surprisingly, the level of expression of Fas 2 after early JNK hyperactivation increased by 20%,
292 in contrast to the reduction observed upon constant JNK hyperactivation (**Figure 7F**). We
293 hypothesize that this increment might be the consequence of the negative impact of Puc on JNK
294 activity. Puc expression would increase in response to the early transient JNK hyperactivation and
295 its activity sustained throughout embryogenesis.

296 In conclusion, the condensation of the VNC and the coordination of the peristaltic movements
297 leading to larval hatching are both dependent on precise levels of JNK activity in pioneer neurons
298 at the beginning of CNS morphogenesis. Early, JNK modulates the establishment of the pioneer
299 landscape and alterations in its activity induce aberrations in the axonal scaffold and in cell bodies
300 positioning. Late, JNK activity impinges upon the final refinement of the allocation of neurons
301 and axonal tracts (**Figure 7H**).

302

303 **DISCUSSION**

304

305 **The embryonic VNC has a robust architecture**

306 During VNC morphogenesis, both neurons and glial cells grow, change shape, and rearrange over
307 time to generate a mechanically balanced structure. Functionally, the neuropile is a well-organized
308 structure, with dendrites of motor and sensory neurons terminating and branching in characteristic
309 domains. Yet, anatomically, it shows few signs of organization, apart from certain regularities such
310 as the commissures and a set of longitudinal axon bundles. This paradox may originate in a
311 shortage of knowledge about the structural cues facilitating networking. We have identified by
312 correlative analyses a series of anchoring positions (nodes) with a potential mechanical role. The
313 nodes consist of sets of Fas 2+ axons organized in a stereotyped 3D conformation that are repeated
314 segment by segment (**Figure 1** and **S1**). We speculate that in architectural terms the longitudinal
315 and commissural connectives serve as structural beams and that nodes may act as cross-points that
316 help to evenly distribute any load from compression, tension or shear that could arise as the VNC
317 forms (or that it may suffer once functional). This robust organization may respond to evolutionary
318 conserved needs in terms of mechanics and physical balance [39] [1]. Of course, the Fas 2+ nodes
319 represent only a subset of the elements holding the tensional network of the VNC, since other Fas
320 2- axons could organize in equivalent structures.

321

322 **The JNK pathway in pioneer neurons modulates VNC architectural organization and**
323 **condensation**

324 Several studies have shown the important function of JNK signaling in axonal plasticity, stability
325 or regeneration [40] [41]. However, its roles in directing CNS morphogenesis or implementing its
326 functional coordination have not been addressed.
327 We found that autonomously increasing JNK activity in early-specified midline VUMs and aCC,
328 pCC and dMP2 pioneers affects the axonal scaffold as a whole (**Figure 5**). These precise neurons
329 are specified and singled out at stage 9 (**Figure 2**) and initiate axonogenesis around stage 11 [34].
330 As the CNS develops, each neuron makes a number of stereotypic pathfinding decisions as they
331 navigate to their particular targets. This is an orchestrated process that in the VNC initiates when
332 the early ipsilateral interneurons MP1, dMP2, vMP2 and pCC, pioneer a scaffold of longitudinal
333 fascicles (stage 12-13). Pioneer axons are subsequently joined by other axons, ipsilateral and
334 contralateral, projecting in anterior or posterior directions. The longitudinal axons fasciculate and

335 defasciculate (stage 14 and 15) in a process in which glial cells intercalate between axonal tracts
336 helping them to distribute in three sets, internal, medial and external in the neuropile (stage 16).
337 At stage 17 the neuron cell bodies positionally relocate and align linearly along the AP axis [42].
338 This lengthy and complex process appears to be affected when JNK activity levels are increased
339 at early stages of development. First, the proper allocation of pioneer neurons along the neuropile
340 and the development of their axonal paths become abnormal. Then, their inaccurate early
341 axonogenesis apparently mislead the fasciculation of other followers' axons that encounter an
342 aberrant guidance landscape. Last, as a result, the execution of the VNC architectural plan and its
343 condensation are challenged (**Figure 7**).

344 Our own data (**Figure 4**) and some data from the literature; e.g. the role of DSCAM regulating
345 circuit level plasticity by inhibiting the receptive field size of retinal bipolar cells [43] point to cell
346 adhesion as an additional major player in the structural organization at a mesoscopic level of the
347 CNS. In particular, changes in the adhesion properties (Fas 2 levels) of pioneer neurons (e.g. RN2
348 and MzVum) upon interference in JNK activity appear to contribute to the global topographical
349 changes observed in the VNC. Fas 2 is involved in homophilic interactions and its deficit leads to
350 fasciculation failures and the disruption of the organization of the local axonal network. The shape
351 and compaction of individual segments is thus affected and, as a consequence, the global
352 architecture and condensation of the VNC perturbed (**Figure 7H**). Such a direct link between JNK
353 signaling and adhesion elements has been noticed in other related scenarios; e.g. in the third instar
354 *Drosophila* larvae, Bsk promotes the axonal pruning of mushroom body gamma neurons by
355 reducing the levels of Fas 2 at the membrane [44]. Although our genetic analyses show that Fas 2
356 is essential for the structural organization and condensation of the VNC, Fas 2 overexpression does
357 not rescue the effects caused by the loss of Puc activity (**Figure 4**).

358 The function of the JNK pathway on the structural organization of the VNC may also involve
359 short-range intercellular communication. Such mechanism has been observed in different
360 developmental, physiological and pathological paradigms. JNK signaling causes non-
361 autonomously patterning changes in imaginal discs [45]. It also induces paracrine compensatory
362 proliferation during regeneration through downstream pathways like Upd, Wg and Dpp [46].
363 Finally, JNK signaling non-autonomously influences tumor microenvironments by affecting the
364 transcription of various cell growth- and proliferation-promoting molecules [47]. A further
365 element involved could be the modulation of cell-cell or cell-matrix contacts. As many as 89 JNK

366 substrates have been described [48], and amongst them are extracellular effectors as Matrix
367 Metalloproteases (MMPs) or integrins). Indeed, in third instar larvae, altering the expression of
368 MMPs or integrins in glial cells results in the elongation of the VNC [49]. Further, integrin mutant
369 phenotypes partially recapitulate the VNC structural defects observed in *puc* mutants [50].
370 Whether any of these elements have any role in the structural organization of the axonal network
371 of the VNC remains to be investigated.

372

373 **JNK signaling coordinates motor activities**

374 In the *Drosophila* embryo, muscles become active very early and isolated twitches and unilateral
375 waves of contraction occur prior to the generation of propagated action potentials [38]. Do the
376 activity of pioneer neurons and the organization of the VNC have any functional significance in
377 this context? Our data strongly advocate for a close relationship between the acquisition of VNC
378 architectural robustness and the rhythmic coordination of motor functions. Mutant embryos of
379 different *puc* alleles and those overexpressing Hep^{CA} in pioneer neurons show severe structural
380 defects and also slower and uncoordinated muscle twitching; they never hatch. This outcome could
381 be explained as an indirect result of firing defects associated to the aberrant dendritic arborizations
382 of pioneer motoneurons (**Figures 5** and **7**) [51]. Our results suggest, however, that muscle
383 coordination failure is primarily linked to the altered organization of the VNC, consequence of
384 pioneer cells malfunction upon early hyperactivation of the JNK pathway (**Figure 7**).

385 Dendrites carry the vast majority of synaptic inputs and their morphology and properties are
386 essential for propagation of postsynaptic potentials [52]. Conceivably, in RN2 neurons, synaptic
387 integration will be affected by those changes in dendritic arborization and morphology associated
388 to high JNK activity. This in turn may alter the frequency or capability of firing action potentials.
389 A remarkable consequence of increasing JNK activity in pioneer motoneurons is the
390 hyperpolarization of their membranes (**Figure 7**) and it is well known that the membrane potential
391 can regulate cell differentiation as well as cortical tissue arrangement, shape and size. Indeed,
392 hyperpolarizing conditions lead to a reduction of the number of connections in immature neurons
393 *in vitro* [53]. Accordingly, in the embryonic VNC, hyperpolarization of RN2 cells after Hep^{CA}
394 overexpression may in part account for their anomalous dendritic arborization. Less probable
395 would be its participation in the implementation of motor coordination. If this were the case,
396 hyperpolarization of RN2 cells should be associated with early hyperactivation of the JNK

397 pathway, which is unlikely.

398

399 **Wiring Optimization**

400 It is well established that spontaneous activities that persistently stimulate postsynaptic cells result
401 in long-term synapse potentiation [54]. These activities propagate efficiently between nearby cells,
402 ensuring connections are strengthened, whereas those from distant ones are lost [55]. Bringing
403 neurons in proximity improves functional interconnectedness and improves wiring optimization
404 [8]. We suggest that these classic principles are followed during the coordination of motor
405 activities in the *Drosophila* embryo. Several arguments support this premise. First, both VNC
406 condensation and motor coordination require a precise level of JNK activity at early developmental
407 stages, enabling activity of pioneer neurons (**Figure 7**). Second, either activation or ablation of the
408 EL interneurons disrupt bilateral muscle contractions in the larvae [56]. Remarkably, these ELs
409 make presynaptic contacts with the RP2 motoneurons, which we found critical for the architectural
410 organization of the VNC and for motor coordination (**Figures 3** and **6**). Third, ELs, and the dorsal
411 projecting motoneurons they innervate, are nearly all *puc*-expressing neurons (**Figure 2**).

412 We foresee that the principles of wiring optimization may also apply at a postembryonic level. As
413 larvae develop, their body wall area grows by two orders of magnitude [57]. To accommodate
414 such a change, the mechanosensory neurons must extend their dendrites and increase their
415 receptive field [58], while motoneurons add more synapses to adapt to larger muscles [57] [59].
416 During scaling, synaptic contacts between nearby neurons are sustained [60]. In this scenario, a
417 post-synaptic neuron can only connect with nearby specific pre-synaptic sites. The propensity to
418 form stable local functional synapses appears to operate across development.

419 Here we uncovered an intimate causal link between the temporal control of the activation of the
420 JNK pathway in pioneer neurons, the structural organization of axonal networks, VNC
421 condensation, and embryonic motor coordination (**Figure 7H**). Correlative geometrical and
422 mechanical studies and further cell type-specific genetic interference analyses will be necessary to
423 dissect the precise mechanisms underlying this process. Yet, wiring optimization across different
424 circuits, by enhancing partners' proximity and topographical robustness, appears to be an essential
425 character associated with morphogenesis of the nervous system.

426

427

428 **METHODS**

429

430 **Drosophila strains**

431 The following stocks were used:

432 *w1118*; *puc^{E69}LacZ/TM3, twi-GFP* [21]

433 *w1118*; *puc^{B48}LacZ/ TM3, twi-GFP* [21]

434 *w1118; UAS-GFP; puc^{E69}I–Gal4/TM6B* [23]

435 *w1118; UAS-GFP; puc^{B48}–Gal4/TM6B* [23]

436 *w1118*; *P{w[+mC]=UAS-bsk.DN}2* (BDSC #6409)

437 *w1118*; *P{w[+mC]=UAS-Hep.Act}2* (BDSC #9306)

438 *P{GawB}elav[C155]* (BDSC #6923)

439 *w1118*; *P{w[+mC]=eve-Gal4.RN2}T, P{w[+mC]=UAS-mCD8::GFP.L}; P{w[+mC]=eve-*
440 *Gal4.RN2}G, P{w[+mC]=UAS-mCD8::GFP.L}* (Dr. Irene Miguel-Aliaga)

441 y*1 w1118*; *P{w[+mC]=CQ2-Gal4}O, P{w[+mC]=UAS-mCD8::GFP.L}LL6* (BDSC #7465)

442 *w1118 P{w[+mW.hs]=GawB}MzVUM; P{y[+t7.7]w[+mC] = 10xUAS-IVS-mCD8::GFP}*
443 *attP40* (Dr. Irene Miguel-Aliaga)

444 *w1118*; *G203:UAS-TNT; ZCL2144* [16] (Dr. Matthias Landgraf)

445 *w1118*; *; ZCL2144* [16] (Dr. Matthias Landgraf)

446 *w1118; P{UAS-syt.eGFP}2* (BDSC #6925)

447 *w1118; UAS-Fas 2^{PEST+}/CyO [Nuc::GFP]* [31] (Dr. Brian McCabe)

448 *w1118, Fas 2^{E76}* (Dr. Brian McCabe)

449 *w1118, Fas 2^{EB112}/FM7[Actin::GFP]* (Dr. Brian McCabe)

450 *w1118, Fas 2-GFP^{CB03616}* (Dr. Christian Klämbt)

451 *w1118; UAS-GFP; HCJ192(iab3)-Gal80 (PS8/13-Gal80)* [30] (Dr. Welcome Bender)

452 In all cases, unless otherwise stated, embryos of the *w1118* strain served as controls.

453

454 **Genetics**

455 All crosses were performed at room temperature and after 48 hours were shifted to different
456 temperatures as the individual experiments required.

457 For temperature shifts, 2 hours embryo collections were done at room temperature in agar plates
458 and aged for a further 2 hours. Then, they were transferred, either to a 29ºC incubator for 4 hours
459 and then to an 18ºC incubator for 12 additional hours [Hep^{CA} (10-13)] or to an 18ºC incubator for
460 12 hours and then to a 29ºC incubator for 4 hours [Hep^{CA} (15-16)]. These timing regimes were
461 calculated to enhance Hep^{CA} expression during the early pioneering stages or during the final cell
462 allocation and axonal refinement stages. After the temperature shifts the embryos were processed
463 for immunocytochemistry or for live imaging.

464

465 **Immunohistochemistry**

466 Immunostaining of flat-prepped stage 16 *Drosophila* embryos was performed using the following
467 primary antibodies: mouse anti-Fas 2 (1:100, clone 1D4, DHSB), mouse anti-axons CNS (1:100,
468 BP 102, DHSB), mouse anti-Futsch (1:1000, 22c10, DHSB), rabbit anti-phospho-JNK (Thr^{183} /
469 Tyr^{185}) (1:100, Cell Signaling #9251), rabbit anti-Dcp-1 (Asp216) (1:100, Cell Signaling #9578),
470 rabbit anti-GFP tag polyclonal (1:600, Thermo Fisher Scientific), rat anti-Elav (1:1000, clone
471 7E8A10, DHSB), mouse anti-Repo (1:100, clone 8D12 DHSB), mouse anti-Even-skipped (1:100,
472 clone 3C10, DHSB), and mouse anti-Engrailed (1:100, clone 4D9, DHSB).

473 The secondary antibodies used for detection were: Goat anti-Rabbit IgG (H+L), Alexa Fluor 488
474 conjugate (A-11008), Goat anti-Rabbit IgG (H+L) Alexa Fluor 555 conjugate (A-21428), Goat
475 anti-Mouse IgG (H+L) Alexa Fluor 488 conjugate (A-11001), Goat anti-Mouse IgG (H+L) Alexa
476 Fluor 555 conjugate (A-21422) and Goat anti-Rat IgG (H+L) Alexa Fluor 555 conjugate (A-
477 21434). All secondary antibodies were used in a dilution of 1:600 and were from Invitrogen.

478

479 **Sample preparations for immunodetection and image acquisition**

480 *Drosophila* embryo dissections for generating flat preparations were performed according to [32].
481 Briefly, flies maintained in apple juice-agar plates at 25ºC were synchronized by repetitive changes
482 of the juice-agar plate, with a time interval of 1.5 hours. All embryos laid within this time window
483 were aged for approximately 22 hours at 18ºC, or until reaching mid-stage 16 (3-part gut stage).
484 At this point embryos were dechorionated with bleach for 1 min, poured into a mesh and rinsed

485 extensively with water. For dissection, embryos were transferred with forceps on the surface of a
486 small piece of double-sided tape, adhered on one of the sides of a poly-L-Lysine coated coverslip.
487 After orienting the embryos dorsal side up and posterior end towards the center of the coverslip,
488 the coverslip was flooded with saline (0.075 M Phosphate Buffer, pH 7.2). Using a pulled glass
489 needle the embryos were manually de-vitelinized and dragged to the center of the coverslip, where
490 they were attached to the coated glass with their ventral side down. An incision on the dorsal side
491 of the embryo was performed using the glass needle from the anterior to the posterior end of the
492 embryo. The gut was removed by mouth suction and a blowing stream of saline was used to flatten
493 their lateral epidermis. Tissue fixation was done with 3.7 % formaldehyde in saline for 10 minutes
494 at room temperature. After this point standard immunostaining procedures were followed.

495 In the single case (**Figure S4**) where whole mount embryos were immunostained, embryo fixation
496 and de-vitelinization was done according to [61]. Both whole mount and flat-prepped
497 immunostained embryos were mounted in Vectashield anti-fading medium (Vector Laboratories,
498 USA).

499 Image acquisition was performed on a Zeiss LSM 700 inverted confocal microscope, using a 63 x
500 oil objective lens (NA 1.4). Z-stacks spanning the whole VNC thickness were acquired applying
501 optimal, with respect to pinhole diameter, sectioning with a step size that varied between 0.2 – 0.6
502 μm. Image processing was performed with Fiji [62].

503

504 **Live imaging**

505 Dechorionated stage 14 embryos were glued ventral side down on a MatTek glass bottom dish and
506 they were covered with S100 Halocarbon Oil (Merck) to avoid desiccation. Image acquisition was
507 performed on a Zeiss LSM 700 inverted confocal microscope, using a 25 X oil immersion lens
508 (N.A 0.8, Imm Korr DIC M27). Z-stacks spanning the whole VNC thickness, with a 2 μm step
509 size, were acquired every 6 minutes for a total of 8 hours. Processing of time-lapse data was done
510 with Fiji [62].

511

512 **Image analysis**

513 Image analysis and quantification of fluorescence intensity were performed using Fiji [62]. In
514 immunostainings where quantification of the fluorescent intensity was required, extra care was

515 taken so that the same antibody batch was used for staining embryos of different genotypes, while
516 identical confocal acquisition settings were applied.

517 For calculating the average integrated density of Fas 2 signal in an image, regions of interest
518 (ROIs) of fixed size were measured at the nodes and internodes positions. Average Integrated
519 Density values obtained by measuring ROIs in several animals (n stated in Figure legends) were
520 then pooled for calculating the mean value as well as standard deviations. For those cases where
521 the quantification of integrated density was performed on a segment basis, the measured values
522 represent the raw integrated density, since the area measured slightly varies in between animals.
523 To calculate the percentage of autonomous and non-autonomous reduction in Fas 2 signal, the
524 GFP signal (RN2 expression) was thresholded and 3D binary masks were created. Masks were
525 employed to delimit the quantification of Fas 2 levels in different domains.

526

527 **Statistical analysis**

528 All statistical analyses were performed using GraphPad Software (GraphPad Software Inc., La
529 Jolla, CA, USA). In all cases one sample t test was performed and probability values $p<0.05$ were
530 considered as significant.

531

532 **Correlations Data analysis**

533 Images were scaled to be isotropic in all axes. Deconvolution was found to not significantly
534 improve the image correlation. Viewed along the AP axis, images were cropped to include only
535 the VNC, and then the VNC was split into 50 bins, corresponding to 1.65 μm length each. Within
536 each bin, a maximum intensity projection was performed along the included (typically eleven)
537 planes in the z-axis. The Matlab function *imregister* was then used to perform the image
538 registration for both inter- and intra- embryo correlations. The optimizer for *imregister* was defined
539 with multimodal metric, tolerance of 10^{-6} and 500 iterations. Before image registration, the center
540 of mass of the two images was aligned so to maximize image overlap. The code was run on a PC
541 with 128 Gb memory and in the most demanding case (full embryo correlation: 50 x 50 = 2500
542 correlations) took around one hour per sample.

543 To create the image correlation traces, the regions of high correlation (e.g. as identified by arrows
544 in **Figure 1**) were manually identified and then plotted considering the mean correlation along ±

545 1 row in the correlation matrices. The diagonal values were ignored. Traces were offset along AP
546 axis to ensure maximum overlap of peaks in the region 25-57 μm to aid comparison between
547 different datasets. In all figures, individual profiles are plotted in gray, with the mean (black) and
548 ± 1 standard deviation (red) shown.

549 To analyze the steepness of the spatial correlations along the AP axis, we created *in silico* data
550 from the real experimental data points - i.e. each *in silico* data point was drawn from a distribution
551 defined by the mean and standard deviation in the samples. We determined the best linear fit to
552 each *in silico* data set and repeated 500 times to find the average gradient fit. This was a robust
553 way to find the steepness as it accounts for experimental noise. To compare between datasets, we
554 defined the variable (where gradient corresponds to the spatial derivative of the correlation along
555 the AP axis):

556 r = (max(gradient) - abs(min(gradient))) / [(max(gradient) + abs(min(gradient)))/2].

557

558 **Muscle contraction analysis**

559 Stage 17 embryos carrying the G203, ZCL2144 or both GFP muscle markers were dechorionated
560 and mounted in halocarbon oil (3:1 mix of S700 and S27) following standard procedures. Muscle
561 contractions were monitored at the embryo's middle plane, using a 25 X oil immersion lens (N.A
562 0.8, Imm Korr DIC M27) in a Zeiss LSM780 confocal microscope. For each acquisition 1000
563 frames were obtained with a scanning speed of 200 msec per frame with a time interval between
564 acquisition cycles of 15 minutes. Muscle activity was monitored up to embryo's hatching or for a
565 total of 12 hours at room temperature. For the experiments where Hep^{CA} over-expression in RN2
566 and MzVum neurons was required, both control and Hep^{CA} overexpressing embryos were filmed
567 at 29°C for equal time periods. For temperature-shift analyses of animals expressing Hep^{CA} in RN2
568 neurons, embryos of equivalent pre-hatching age were recorded at 200 msec per frame for 500
569 frames. Post-imaging, movies were processed with Fiji [62] and Kymographs were generated
570 using the Fiji plugin KymoResliceWide.

571

572 **Axonal Trafficking**

573 To examine axonal trafficking, stage 17 embryos expressing UAS-Syt-GFP were dechorionated
574 and mounted laterally in halocarbon oil (3:1 mix of S700 and S27) for live imaging. Synaptic

575 vesicle transport was monitored in the medial part of the Inter-Segmental Nerve (ISN) using a 40
576 X oil immersion lens (N.A 1.3, Oil DIC M27) in a Zeiss LSM780 confocal microscope. A constant
577 frame size of 512x100 pixels, with an XY zoom of 6 and a recording line spacing of 2 were
578 routinely employed. Single plane movies were acquired with a scanning speed of 1.11 sec, with 1
579 sec interval for a total of 60 cycles. All movies were processed with Fiji and Kymographs were
580 generated using the Fiji plugin KymoResliceWide.

581 The Mean Velocity and the Lifetime parameters for each particle were calculated from the
582 Kymographs as follows. The particles trajectories were traced and saved as independent ROIs. The
583 XY coordinates for each ROI were then extracted using the getSelectionCoordinates function in
584 Fiji of the custom made "Macro coordinates.ijm" shown below:

```
585 run("Fit Spline", "straighten");
586   getSelectionCoordinates(x, y);
587   x2=0; y2=0; distance=0;
588   for (i=0; i<x.length; i++) {
589       if (i>0) {
590           dx = x[i] - x[i-1];
591           dy = y[i] - y[i-1];
592           distance = sqrt(dx*dx+dy*dy);
593       }
594       print(i, x[i], y[i], distance);
595   }
```

596 These XY coordinates represent the particles displacement in both space (X values) and time (Y
597 values), thus permitting the calculation of Mean Velocity and Lifetime.

598

599 **Analysis of Axonal and dendrite morphology by Segmentation**

600 To describe the axonal and dendrite morphology of the RN2+ neurons, we analyzed images of flat-
601 prepped embryos immunostained against GFP and Fasciclin 2 using the Simple Neurite Tracer Fiji
602 plugin [63]. Image segmentation by this tool allows a semi-automated tracing of axons and

603 dendrites in 3D, providing measurements of total axonal and dendrite length, as well as of dendrite
604 number directly from skeletonized images.
605
606 **Western Blotting**
607 Dechorionated stage 16 embryos of the *puc^{E69}LacZ / TM3, twi-GFP* and *puc^{B48}LacZ / TM3, twi-*
608 *GFP* lines were used for generating whole embryo extracts for western blot analysis. In detail,
609 homozygous embryos were separated from their balanced siblings under a fluorescent dissecting
610 scope based on the *twi-GFP* expression. Approximately 100 embryos of each type were fully
611 homogenized in 100 µL of iced cold RIPA buffer, supplemented with Protease Inhibitors (Protease
612 Inhibitor Cocktail Tablets, Roche Life Sciences). Subsequently, the extracts were centrifuged at
613 3500 g for 15 minutes at 4ºC and the supernatants were collected. Total protein concentration in
614 the lysates was determined by Bradford assay (Bio-Rad) and 30 µg of sample were analyzed in a
615 10 % SDS-PAGE. Proteins were blotted on Protran nitrocellulose membrane (Whatman) while the
616 antibodies employed were: anti-Fas 2 (1:1000, clone 1D4, DSHB) and Pan-actin (1:1000, Cell
617 Signaling). The ECL Plus chemiluminescent substrate (Pierce, Thermo Fisher Scientific) was used
618 for antibody detection. Western Blot signal quantification was performed with Fiji by measuring
619 the average density of each band.
620
621 **Embryo whole-cell patch-clamp recordings**
622 Dissections and recordings were performed as described[38] at room temperature (20-22°C). Late
623 stage 17 *Drosophila* embryos were dissected in external saline (in mM: 135 NaCl, 5 KCl, 4
624 MgCl2·6H2O, 2 CaCl2·2H2O, 5 N-Tris[hydroxymethyl]methyl-2-aminoethanesulfonic acid, and
625 36 sucrose, pH 7.15). The CNS was exposed through a dorsal-longitudinal cut of the dechorionated
626 embryonic body wall musculature. Embryonic cuticle was secured to a Sylgard (Dow-Corning,
627 Midland, Michigan, USA)-coated cover slip using tissue glue (GLUture; WPI, Hitchin, UK) and
628 larval gut and fat body removed. The glia surrounding the CNS was partially removed using
629 protease (1% type XIV; Sigma, Dorset, UK) contained in a wide-bore (15 µm) patch pipette.
630 Whole cell recordings were carried out using borosilicate glass electrodes (GC100TF-10; Harvard
631 Apparatus, Edenbridge, UK), fire-polished to resistances of between 16-20 MΩ. Cell identity was
632 confirmed through RN2-GAL4 driven expression of UAS-CD8-GFP. Recordings were made

using a MultiClamp 700B amplifier. Endogenous excitatory synaptic cholinergic input to the aCC/RP2 motoneurons were recorded in voltage clamp and current clamp sampled at 20 kHz and low pass filtered at 10 kHz, using pClamp 10.6 (Molecular Devices, Sunnyvale, CA). Only neurons with an input resistance of ≥ 1GΩ were accepted for analysis.

ACKNOWLEDGEMENTS

We are extremely grateful to all colleagues that have provided us materials, training and guidance throughout this work as well as for commenting on the manuscript. Amongst them we like to specially thank Elisabeth Knust, Christian Klambt, Claude Desplan, Matthias Landgraf, Chris Doe, Andreas Prokop, Natalia Sanchez-Soriano, Alicia Hidalgo, Marta Zlatic, Albert Cardona, Brian McCabe and Irene Miguel-Aliaga. We also thank our colleagues at the Parc Cientific de Barcelona, the Mechanobiology Institute of Singapore and the BSRC "Alexander Fleming" of Athens for their constant encouragement and support. The Martín-Blanco laboratory was supported by funds from Programa Estatal de Fomento de la Investigación Científica y Técnica de Excelencia (BFU2014-57019-P and BFU2017-82876-P) and from Fundación Ramón Areces. TES was supported by a Singapore National Research Foundation Fellowship (NRF2012NRF-NRFF001-094) and core support from the Mechanobiology Institute. RAB was supported by a Biotechnology and Biological Sciences Research Council grant (BBSRC BB/L027690/1) and SWV by a BBSRC CASE studentship. Work on this project benefited from the Manchester Fly Facility, established through funds from University and the Wellcome Trust (087742/Z/08/Z).

658 **REFERENCES**

659

660 1. Arendt D, Tosches MA, Marlow H. From nerve net to nerve ring, nerve cord and brain--
661 evolution of the nervous system. Nature reviews Neuroscience. 2016;17(1):61-72. doi:
662 10.1038/nrn.2015.15.
663 2. Qing Yu ZL, Chuanzi OuYang, Lingjun Li. Biologically Active Peptides in Invertebrates:
664 Discovery and Functional Studies. Colloqium Series on neuropeptides: Morgan & Claypool
665 Publishers; 2015. p. 182.
666 3. Leise EM. Modular construction of nervous systems: a basic principle of design for
667 invertebrates and vertebrates. Brain research Brain research reviews. 1990;15(1):1-23.
668 4. Chen BL, Hall DH, Chklovskii DB. Wiring optimization can relate neuronal structure and
669 function. Proceedings of the National Academy of Sciences of the United States of America.
670 2006;103(12):4723-8. doi: 10.1073/pnas.0506806103.
671 5. Redies C, Puelles L. Modularity in vertebrate brain development and evolution. BioEssays
672 : news and reviews in molecular, cellular and developmental biology. 2001;23(12):1100-11. doi:
673 10.1002/bies.10014.
674 6. Sporns O, Betzel RF. Modular Brain Networks. Annu Rev Psychol. 2016;67:613-40. doi:
675 10.1146/annurev-psych-122414-033634.
676 7. Huntenburg JM. A core organizing axis of the human cerebral cortex: PhD Thesis. Freie
677 Universität Berlin; 2018.
678 8. Cajal SRy. Textura del Sistema Nervioso del Hombre y de los Vertebrados. Madrid, Spain:
679 Nicolas Moya; 1899.
680 9. Tessier-Lavigne M, Goodman CS. The molecular biology of axon guidance. Science.
681 1996;274(5290):1123-33.
682 10. Chklovskii DB, Koulakov AA. Maps in the brain: what can we learn from them? Annual
683 review of neuroscience. 2004;27:369-92. doi: 10.1146/annurev.neuro.27.070203.144226.
684 11. Huntenburg JM, Bazin PL, Margulies DS. Large-Scale Gradients in Human Cortical
685 Organization. Trends Cogn Sci. 2018;22(1):21-31. doi: 10.1016/j.tics.2017.11.002.
686 12. Technau GM. Brain development in Drosophila melanogaster: Springer Science+Business
687 Media, LLC - Landes Bioscience; 2008.

688 13. Landgraf M, Sanchez-Soriano N, Technau GM, Urban J, Prokop A. Charting the
689 Drosophila neuropile: a strategy for the standardised characterisation of genetically amenable
690 neurites. Developmental biology. 2003;260(1):207-25.
691 14. Crisp SJ, Evers JF, Bate M. Endogenous patterns of activity are required for the maturation
692 of a motor network. J Neurosci. 2011;31(29):10445-50. doi: 10.1523/JNEUROSCI.0346-11.2011.
693 15. Suster ML, Bate M. Embryonic assembly of a central pattern generator without sensory
694 input. Nature. 2002;416(6877):174-8. doi: 10.1038/416174a.
695 16. Crisp S, Evers JF, Fiala A, Bate M. The development of motor coordination in Drosophila
696 embryos. Development. 2008;135(22):3707-17. doi: 10.1242/dev.026773.
697 17. Lin DM, Fetter RD, Kopczynski C, Grenningloh G, Goodman CS. Genetic analysis of
698 Fasciclin II in Drosophila: defasciculation, refasciculation, and altered fasciculation. Neuron.
699 1994;13(5):1055-69.
700 18. Kolodkin AL, Tessier-Lavigne M. Mechanisms and molecules of neuronal wiring: a
701 primer. Cold Spring Harbor perspectives in biology. 2011;3(6):a001727.
702 19. Srahna M, Leyssen M, Choi CM, Fradkin LG, Noordermeer JN, Hassan BA. A signaling
703 network for patterning of neuronal connectivity in the Drosophila brain. PLoS biology.
704 2006;4(11):e348. doi: 10.1371/journal.pbio.0040348.
705 20. Koch M, Nicolas M, Zschaetzsch M, de Geest N, Claeys A, Yan J, et al. A Fat-Facets-
706 Dscam1-JNK Pathway Enhances Axonal Growth in Development and after Injury. Front Cell
707 Neurosci. 2017;11:416. doi: 10.3389/fncel.2017.00416.
708 21. Martin-Blanco E, Gampel A, Ring J, Virdee K, Kirov N, Tolkovsky AM, et al. puckered
709 encodes a phosphatase that mediates a feedback loop regulating JNK activity during dorsal closure
710 in Drosophila. Genes & development. 1998;12(4):557-70.
711 22. Martin-Blanco E. Regulatory control of signal transduction during morphogenesis in
712 Drosophila. The International journal of developmental biology. 1998;42(3):363-8.
713 23. Pastor-Pareja JC, Grawe F, Martin-Blanco E, Garcia-Bellido A. Invasive cell behavior
714 during Drosophila imaginal disc eversion is mediated by the JNK signaling cascade. Dev Cell.
715 2004;7(3):387-99. doi: 10.1016/j.devcel.2004.07.022.
716 24. Shklover J, Mishnaevski K, Levy-Adam F, Kurant E. JNK pathway activation is able to
717 synchronize neuronal death and glial phagocytosis in Drosophila. Cell death & disease.
718 2015;6:e1649. doi: 10.1038/cddis.2015.27.

719 25. Foty RA, Steinberg MS. The differential adhesion hypothesis: a direct evaluation.
720 Developmental biology. 2005;278(1):255-63. doi: 10.1016/j.ydbio.2004.11.012.
721 26. Amack JD, Manning ML. Knowing the boundaries: extending the differential adhesion
722 hypothesis in embryonic cell sorting. Science. 2012;338(6104):212-5. doi:
723 10.1126/science.1223953.
724 27. Grenningloh G, Rehm EJ, Goodman CS. Genetic analysis of growth cone guidance in
725 Drosophila: fasciclin II functions as a neuronal recognition molecule. Cell. 1991;67(1):45-57.
726 28. Neuert H, Deing P, Krukkert K, Naffin E, Steffes G, Risse B, et al. The Drosophila NCAM
727 homolog Fas 2 signals independently of adhesion. Development. 2020;147(2). Epub 2019/12/22.
728 doi: 10.1242/dev.181479.
729 29. Zhang S, Amourda C, Garfield D, Saunders TE. Selective Filopodia Adhesion Ensures
730 Robust Cell Matching in the Drosophila Heart. Dev Cell. 2018;46(2):189-203 e4. Epub
731 2018/07/18. doi: 10.1016/j.devcel.2018.06.015.
732 30. Bowman SK, Deaton AM, Domingues H, Wang PI, Sadreyev RI, Kingston RE, et al.
733 H3K27 modifications define segmental regulatory domains in the Drosophila bithorax complex.
734 Elife. 2014;3:e02833. Epub 2014/08/02. doi: 10.7554/eLife.02833.
735 31. Beck ES, Gasque G, Imlach WL, Jiao W, Jiwon Choi B, Wu PS, et al. Regulation of
736 Fasciclin II and synaptic terminal development by the splicing factor beag. J Neurosci.
737 2012;32(20):7058-73. Epub 2012/05/18. doi: 10.1523/JNEUROSCI.3717-11.2012.
738 32. Landgraf M, Bossing T, Technau GM, Bate M. The origin, location, and projections of the
739 embryonic abdominal motorneurons of Drosophila. J Neurosci. 1997;17(24):9642-55.
740 33. Furrer MP, Vasenkova I, Kamiyama D, Rosado Y, Chiba A. Slit and Robo control the
741 development of dendrites in Drosophila CNS. Development. 2007;134(21):3795-804. doi:
742 10.1242/dev.02882.
743 34. Jacobs JR, Goodman CS. Embryonic development of axon pathways in the Drosophila
744 CNS. II. Behavior of pioneer growth cones. J Neurosci. 1989;9(7):2412-22.
745 35. Sink H, Whitington PM. Pathfinding in the central nervous system and periphery by
746 identified embryonic Drosophila motor axons. Development. 1991;112(1):307-16.
747 36. Pereanu W, Spindler S, Im E, Buu N, Hartenstein V. The emergence of patterned
748 movement during late embryogenesis of Drosophila. Dev Neurobiol. 2007;67(12):1669-85. doi:
749 10.1002/dneu.20538.

750 37. Baines RA, Robinson SG, Fujioka M, Jaynes JB, Bate M. Postsynaptic expression of
751 tetanus toxin light chain blocks synaptogenesis in Drosophila. Curr Biol. 1999;9(21):1267-70.
752 38. Baines RA, Bate M. Electrophysiological development of central neurons in the Drosophila
753 embryo. J Neurosci. 1998;18(12):4673-83.
754 39. Matheson T. Invertebrate Nervous Systems. Encyclopedia of Life Sciences. 2002:1-6.
755 40. Hartwig CL, Worrell J, Levine RB, Ramaswami M, Sanyal S. Normal dendrite growth in
756 Drosophila motor neurons requires the AP-1 transcription factor. Dev Neurobiol.
757 2008;68(10):1225-42. doi: 10.1002/dneu.20655.
758 41. Vonhoff F, Kuehn C, Blumenstock S, Sanyal S, Duch C. Temporal coherency between
759 receptor expression, neural activity and AP-1-dependent transcription regulates Drosophila
760 motoneuron dendrite development. Development. 2013;140(3):606-16. doi: 10.1242/dev.089235.
761 42. Hartenstein V. Atlas of Drosophila development: Cold Spring Harbor Laboratory Press;
762 1993.
763 43. Simmons AB, Bloomsburg SJ, Sukeena JM, Miller CJ, Ortega-Burgos Y, Borghuis BG, et
764 al. DSCAM-mediated control of dendritic and axonal arbor outgrowth enforces tiling and inhibits
765 synaptic plasticity. Proceedings of the National Academy of Sciences of the United States of
766 America. 2017;114(47):E10224-E33. Epub 2017/11/09. doi: 10.1073/pnas.1713548114.
767 44. Bornstein B, Zahavi EE, Gelley S, Zoosman M, Yaniv SP, Fuchs O, et al. Developmental
768 Axon Pruning Requires Destabilization of Cell Adhesion by JNK Signaling. Neuron.
769 2015;88(5):926-40. doi: 10.1016/j.neuron.2015.10.023.
770 45. Ahmed-de-Prado S, Diaz-Garcia S, Baonza A. JNK and JAK/STAT signalling are required
771 for inducing loss of cell fate specification during imaginal wing discs regeneration in Drosophila
772 melanogaster. Developmental biology. 2018;441(1):31-41. Epub 2018/06/06. doi:
773 10.1016/j.ydbio.2018.05.021.
774 46. Pinal N, Calleja M, Morata G. Pro-apoptotic and pro-proliferation functions of the JNK
775 pathway of Drosophila: roles in cell competition, tumorigenesis and regeneration. Open Biol.
776 2019;9(3):180256. Epub 2019/03/07. doi: 10.1098/rsob.180256.
777 47. La Marca JE, Richardson HE. Two-Faced: Roles of JNK Signalling During
778 Tumourigenesis in the Drosophila Model. Front Cell Dev Biol. 2020;8:42. Epub 2020/03/03. doi:
779 10.3389/fcell.2020.00042.

780 48. Bogoyevitch MA, Kobe B. Uses for JNK: the many and varied substrates of the c-Jun N-
781 terminal kinases. Microbiol Mol Biol Rev. 2006;70(4):1061-95. Epub 2006/12/13. doi:
782 10.1128/MMBR.00025-06.
783 49. Meyer S, Schmidt I, Klambt C. Glia ECM interactions are required to shape the Drosophila
784 nervous system. Mech Dev. 2014;133:105-16. Epub 2014/05/27. doi: 10.1016/j.mod.2014.05.003.
785 50. Stevens A, Jacobs JR. Integrins regulate responsiveness to slit repellent signals. J Neurosci.
786 2002;22(11):4448-55. Epub 2002/06/01. doi: 20026413.
787 51. Katz LC, Shatz CJ. Synaptic activity and the construction of cortical circuits. Science.
788 1996;274(5290):1133-8.
789 52. Spruston N, Stuart G, Häusser M. Principles of dendritic integration. In: Spruston N, Stuart
790 G, Häusser M, editors. Dendrites. Oxford: Oxford University Press; 2016.
791 53. Ozkucur N, Quinn KP, Pang JC, Du C, Georgakoudi I, Miller E, et al. Membrane potential
792 depolarization causes alterations in neuron arrangement and connectivity in cocultures. Brain
793 Behav. 2015;5(1):24-38. doi: 10.1002/brb3.295.
794 54. Hebb D. The Organization of Behavior: A Neuropsychological Theory. John Wiley And
795 Sons Inc; New York; Chapman And Hall Limited; London; 1949.
796 55. Eglen SJ, Demas J, Wong RO. Mapping by waves. Patterned spontaneous activity regulates
797 retinotopic map refinement. Neuron. 2003;40(6):1053-5.
798 56. Heckscher ES, Zarin AA, Faumont S, Clark MQ, Manning L, Fushiki A, et al. Even-
799 Skipped(+) Interneurons Are Core Components of a Sensorimotor Circuit that Maintains Left-
800 Right Symmetric Muscle Contraction Amplitude. Neuron. 2015;88(2):314-29. doi:
801 10.1016/j.neuron.2015.09.009.
802 57. Keshishian H, Chiba A. Neuromuscular development in Drosophila: insights from single
803 neurons and single genes. Trends Neurosci. 1993;16(7):278-83.
804 58. Grueber WB, Jan LY, Jan YN. Tiling of the Drosophila epidermis by multidendritic
805 sensory neurons. Development. 2002;129(12):2867-78.
806 59. Rasse TM, Fouquet W, Schmid A, Kittel RJ, Mertel S, Sigrist CB, et al. Glutamate receptor
807 dynamics organizing synapse formation in vivo. Nat Neurosci. 2005;8(7):898-905.
808 60. Gerhard S, Andrade I, Fetter RD, Cardona A, Schneider-Mizell CM. Conserved neural
809 circuit structure across Drosophila larval development revealed by comparative connectomics.
810 Elife. 2017;6. doi: 10.7554/eLife.29089.

811 61. Patel NH. Imaging neuronal subsets and other cell types in whole-mount Drosophila
812 embryos and larvae using antibody probes. Methods in cell biology. 1994;44:445-87.
813 62. Schindelin J, Arganda-Carreras I, Frise E, Kaynig V, Longair M, Pietzsch T, et al. Fiji: an
814 open-source platform for biological-image analysis. Nat Methods. 2012;9(7):676-82. doi:
815 10.1038/nmeth.2019.
816 63. Longair MH, Baker DA, Armstrong JD. Simple Neurite Tracer: open source software for
817 reconstruction, visualization and analysis of neuronal processes. Bioinformatics.
818 2011;27(17):2453-4. doi: 10.1093/bioinformatics/btr390.
819
820

821 **FIGURES**

Figure 1

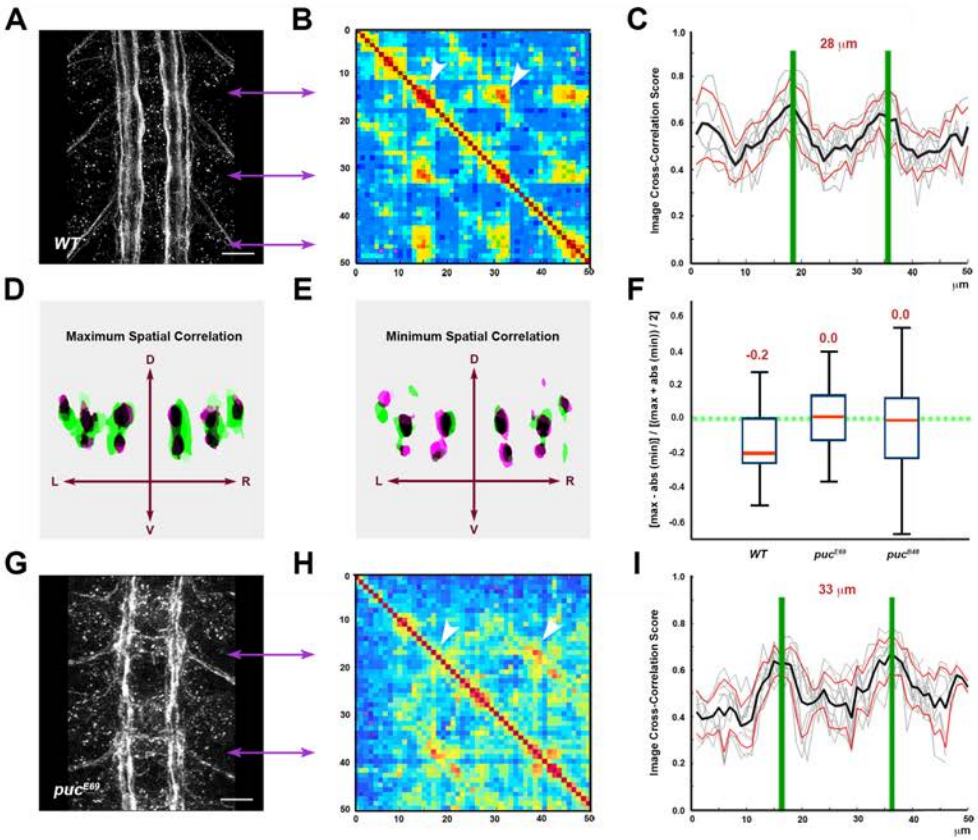
A
B
C
WT
28 μm
Image Cross-Correlation Score
μm
D
E
F
Maximum Spatial Correlation
Minimum Spatial Correlation
D
L
R
V
-0.2
0.0
0.0
[max - abs (min)] / [(max + abs (min)) / 2]
WT
G
H
I
33 μm
Image Cross-Correlation Score
μm

822

823 **Figure 1. Structural Architecture of the Ventral Nerve Cord (VNC) of the *Drosophila***
824 **embryo**

825 **A)** Maximum projection of the VNC of a stage 16 *wt* embryo stained with Fas 2. See **Movie S1**.
826 Scale Bar is 10 μm.

827 **B)** Self cross-correlation matrix of the Z sections of the image in **A** along the AP axis. The color-
828 coded representation, in all figures from now on, shows the correlation level for each possible
829 comparison at each position along the AP axis. In this way, it was possible to identify an oscillatory
830 pattern of hot spots (3D nodes - purple double headed arrows) of high correlation. One conspicuous
831 node of robust correlation per segment was detected (white arrowheads).

832 **C)** Image cross-correlation score along the AP axis for **B** (n=6). The cross-correlation profile
833 shows that segmental Fas 2 nodes fell 28 μm apart in *wt* animals and that the internodal maximum
834 noise/minimum correlation maps 9 μm posterior to the node. The grey lines show individual
835 profiles. The black line corresponds to Average values and the red lines to Standard Deviations.
836 The green bars indicate the positions of maximum correlation (nodes).

837 **D)** Z sections at two different maximal (green and magenta) correlation positions (from **A**)
838 showing coalescence of Fas 2 connectives at the nodes. DV and ML [Left (L) and R (Right)] axes
839 are indicated by arrows.

840 **E)** Z sections at two different minimal (green and magenta) correlation positions (from **A**) showing
841 dispersion and stochastic distribution associated to internodal noise. DV and ML [Left (L) and R
842 (Right)] axes are indicated by arrows.

843 **F)** Box plots of the gradient of the spatial correlation along the AP axis, normalized by the
844 difference between the maximum and minimum gradients for *wt,* puc^{E69} and puc^{B48} individuals.
845 Boxes denote 95% confidence interval. The mutant values were not distinguishable from zero.

846 **G)** Equivalent image to **A** for a puc^{E69} embryo. Note the defasciculation and collapse of the
847 longitudinal connectives, specially the most lateral ones. See **Movie S2**. Scale Bar is 10 μm.

848 **H)** Self cross-correlation matrix of the Z sections of the image in **D**. In puc^{E69} mutants, while
849 correlation matrices are noisier, a single node per segment can still be observed (white
850 arrowheads).

851 **I)** Image cross-correlation score along the AP axis for **E** (n=9). Segmental Fas 2 nodes spread 33
852 μm away in puc^{E69} and the internodal minima gets diffuse. Lines and bars are coded as in **C**.

Figure 2

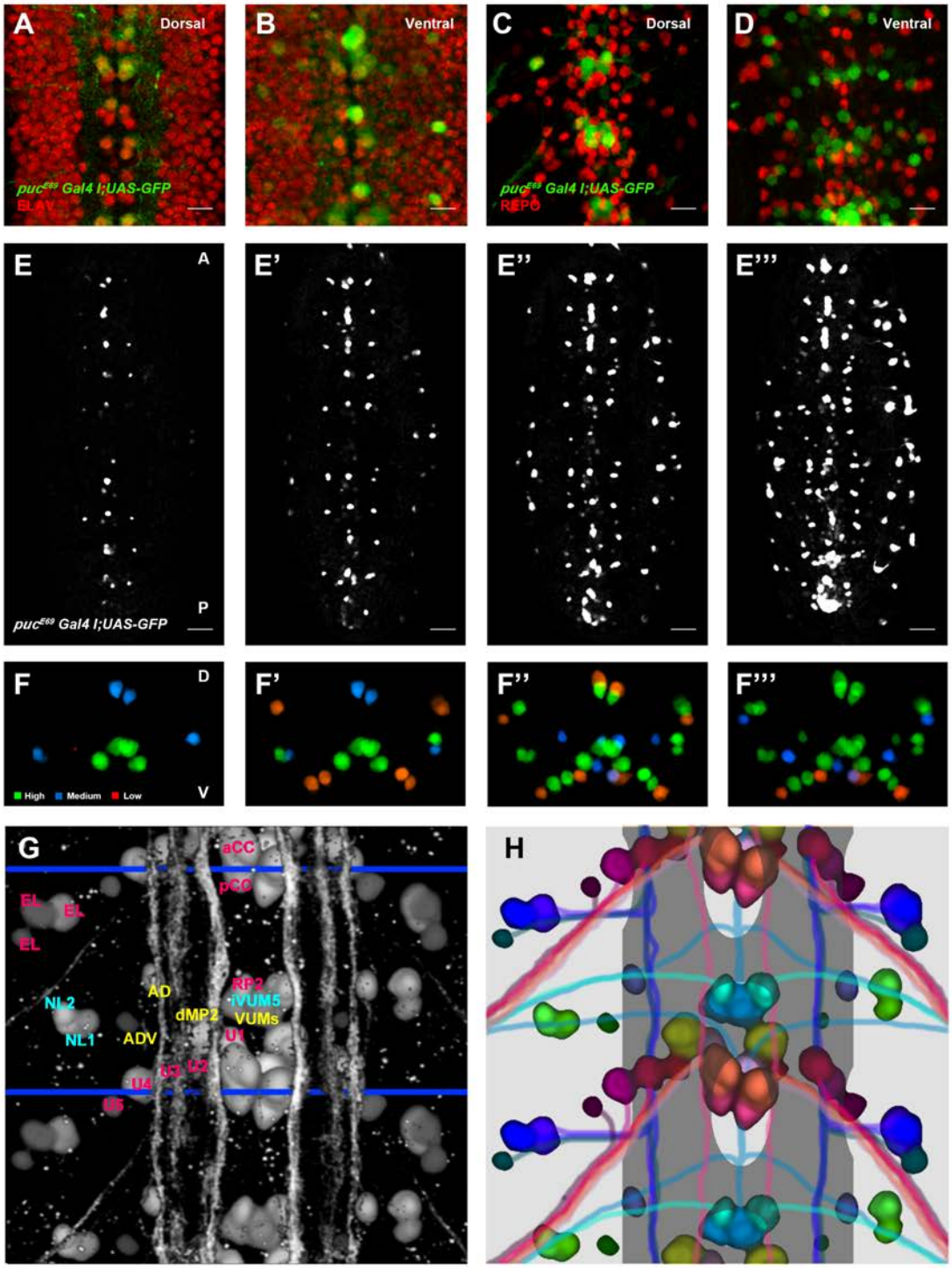
A
Dorsal
puc^{E69} Gal4 I;UAS-GFP
ELAV
B
Ventral
C
Dorsal
puc^{E69} Gal4 I;UAS-GFP
REPO
D
Ventral
E
A
P
puc^{E69} Gal4 I;UAS-GFP
E'
E''
E'''
F
D
V
High
Medium
Low
F'
F''
F'''
G
aCC
pCC
EL
EL
EL
NL2
NL1
AD
ADV
dMP2
RP2
iVUM5
VUMs
U1
U2
U3
U4
U5
H

853

854 **Figure 2. JNK signaling is dynamically regulated during development**

855 **A** to **D)** Dorsal and ventral sections highlighting the expression of *puc* (green) in the VNC of stage
856 17 *puc*^{E69}*I-Gal4 > UAS-GFP* embryo double-stained for the pan-neuronal marker Elav (**A** and **B**
857 - red) or the glial marker Repo (**C** and **D** - red). *puc* is expressed in a subset of neurons in each
858 segment but not in glia. Scale Bar is 10 µm.

859 **E** to **E''')** four different snapshots from **Movie S3** at the indicated time points from the UAS-GFP;
860 *puc*^{E69}*I*-Gal4 viable line. *puc* expression can be observed from early stage 13 in a few neurons at
861 midline. As development progressed, more and more neurons express *puc*. Scale Bar is 10 µm.

862 **F** to **F''')** Diagram displaying the cumulative expression of *puc* at the same time points as in **E** to
863 **E'''**. A minimum consensus of 19 neurons per hemisegment was defined. At each time point the
864 intensity (defined by visual inspection) was displayed as low (red), medium (blue) and high (green)
865 (see also **Movie S4**).

866 **G)** Composition summarizing the expression of *puc* in the CNS [*puc* expressing cells in the VNC
867 at stage 16 including those identified by coexpressing Even-skipped (magenta) or Engrailed (cyan)
868 plus those putatively identified by morphological and positional criteria (yellow - AD, ADV,
869 dMP2 and 2 VUM En-negative motor neurons)]. To facilitate understanding, a scaled Fas 2
870 expression image from an embryo of the same stage was overimposed to the diagram. Positions of
871 the robustness nodes are highlighted as dark blue lines.

872 **H)** Diagram representing the whole set of *puc* expressing cells (compare to G) and their expected
873 axonal contributions to connectives and exiting nerves (each individual cell carried a single color-
874 code). This diagram was over-imposed over a grey mask covering the scaled width and shape of
875 the VNC.

Figure 3

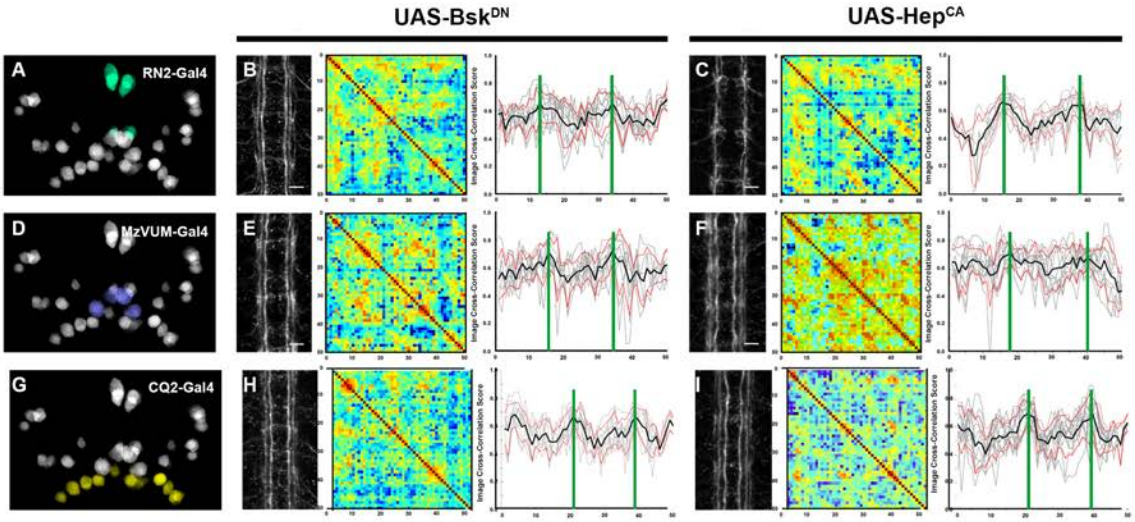
UAS-Bsk^{DN}
UAS-Hep^{CA}
A
RN2-Gal4
B
C
D
MzVUM-Gal4
E
F
G
CQ2-Gal4
H
I
Image Cross-Correlation Score

876

877 **Figure 3. Targeted activation and inhibition of the JNK pathway in the VNC**

878 **A)** Cartoon representing the full set of *puc* expressing neurons per segment in the VNC
879 highlighting the cells expressing RN2-Gal4 (turquoise).

880 **B** and **C)** From left to right, pattern of Fas 2 expression, self-cross-correlation matrix and image
881 cross-correlation profiles for VNCs of 16-stage embryos upon expression of UAS-Bsk^{DN} **(B)** and
882 UAS-Hep^{CA} **(C)** transgenes under the control of the RN2-Gal4 respectively, inhibiting and
883 hyperactivating JNK activity in the aCC, pCC and RP2 cells. These conditions affect connectives
884 defasciculation, nodes profiles and VNC condensation. Scale Bar is 10 µm.

885 **D)** Cartoon highlighting the *puc*+ neurons expressing MzVum-Gal4 (purple).

886 **E** and **F)** As **B** and **C** but employing MzVum-Gal4 for interfering in JNK activity in the VUM
887 neurons. Affecting JNK activity levels in VUMs also affects defasciculation, nodes profiles and
888 condensation. Scale Bar is 10 µm.

889 **G)** Cartoon highlighting the *puc*+ cells expressing CQ2-Gal4 (yellow).

890 **H** and **I)** As **B** and **C** but employing CQ2-Gal4 for interfering in JNK activity in the U
891 motoneurons. None of these conditions result in noticeable defects. Scale Bar is 10 µm.

Figure 4

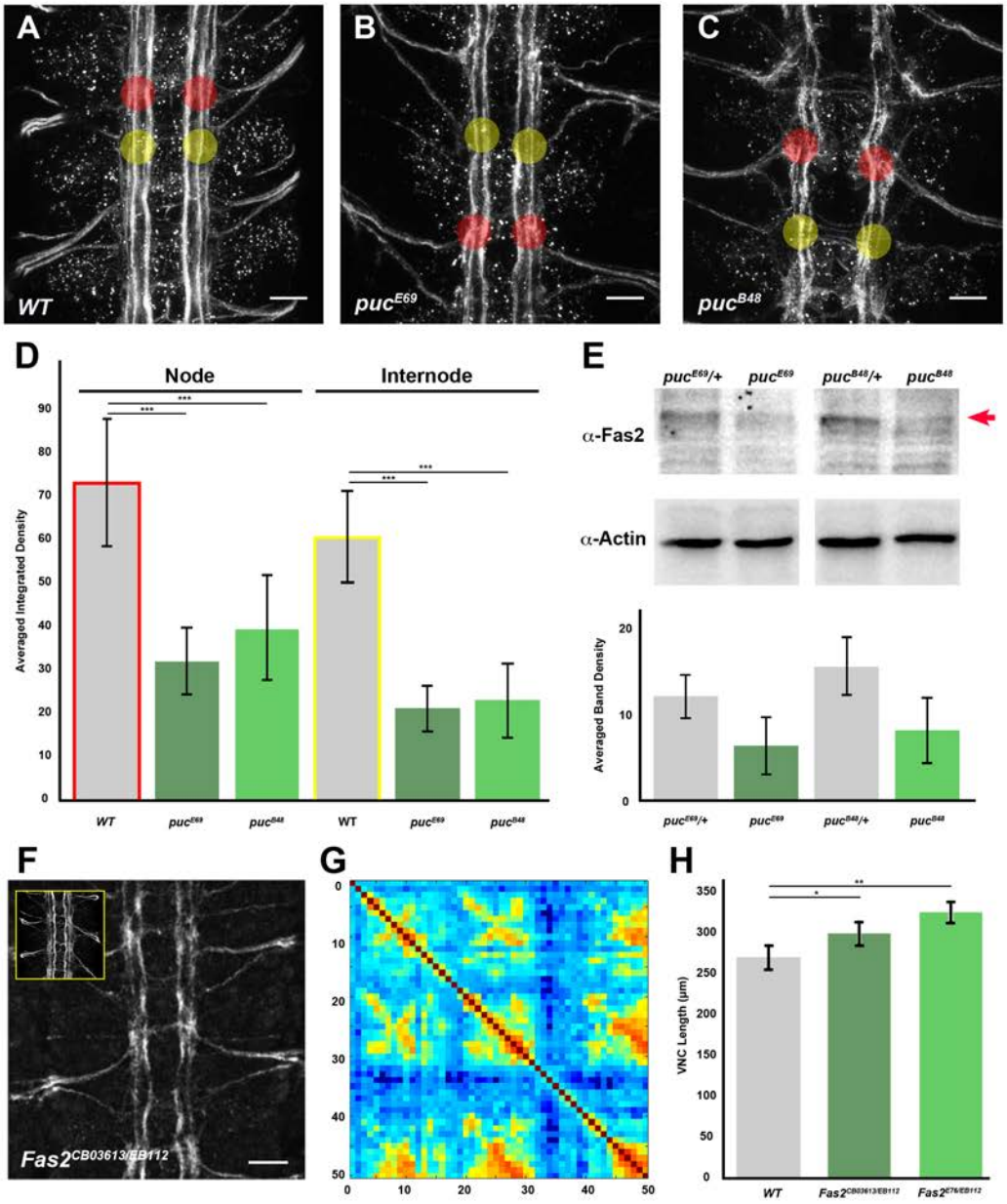
A
WT
B
puc^E69
C
puc^B48
D
Node
Internode
Averaged Integrated Density
WT
puc^E69
puc^B48
E
puc^E69/+
puc^E69
puc^B48/+
puc^B48
α-Fas2
α-Actin
Averaged Band Density
F
Fas2^CB03613/EB112
G
H
VNC Length (μm)
WT
Fas2^CB03613/EB112
Fas2^E76/EB112

892

893 **Figure 4. Fasciclin 2 is necessary for VNC condensation and its expression is modulated by**
894 **the JNK pathway**

895 **A)** *wt*, **B)** puc^{E69} and **C)** puc^{B48} stage 16 embryos Fas 2 immunoreactivity. Maximum projection of
896 ventral views across three VNC abdominal segments. Overlaid circles represent the fixed area
897 ROIs used for measuring the Average Integrated Density of Fas 2 signal, either at the node (red)
898 or at the internode (yellow) positions. Scale Bar is 10 µm.

899 **D)** Quantification of the Average Integrated Density of Fas 2 signal at node and internode positions
900 as indicated. Statistically significant differences in Fas 2 levels ($p < 0.0001$) were detected between
901 *wt* and *puc* embryos, both at the node and internode positions.

902 **E)** Immunodetection of Fas 2 in extracts from stage 16 *puc* embryos. Extracts of balanced siblings
903 were used as controls. In control extracts, the antibody against Fas 2 detected a strong band at 95
904 kD (red arrow), the intensity of which was reduced by half in extracts from *puc* homozygous
905 embryos. Detection of actin (42 kD) served as loading control for the quantification of the Fas 2
906 signal. The graph represents the averaged Fas 2 band intensities normalized with respect to actin.

907 **F)** Fas 2-GFP expression pattern of a stage 16 embryo mutant for Fas 2 ($Fas\ 2^{CB03613}$ / $Fas\ 2^{EB112}$).
908 Maximum projection of ventral views across three VNC abdominal segments. A general
909 derangement of the axonal network was observed [compare to the Fas 2-GFP expression pattern
910 of a stage 16 heterozygous embryo ($Fas\ 2^{CB03613}$ / +) (inset)]. Scale Bar is 10 µm.

911 **G)** Self cross-correlation matrix along the A/P axis of the Z sections of the image in **F**. The color-
912 coded representation shows the correlation level at each axial position. One spread node per
913 segment was detected.

914 **H)** Quantification of the VNC length in µm (average and standard deviation) for each condition.
915 Statistically significant differences in length ($p < 0.01$ and $p < 0.001$) were detected between the
916 *wt* and the different *Fas 2* allelic combinations.

Figure 5

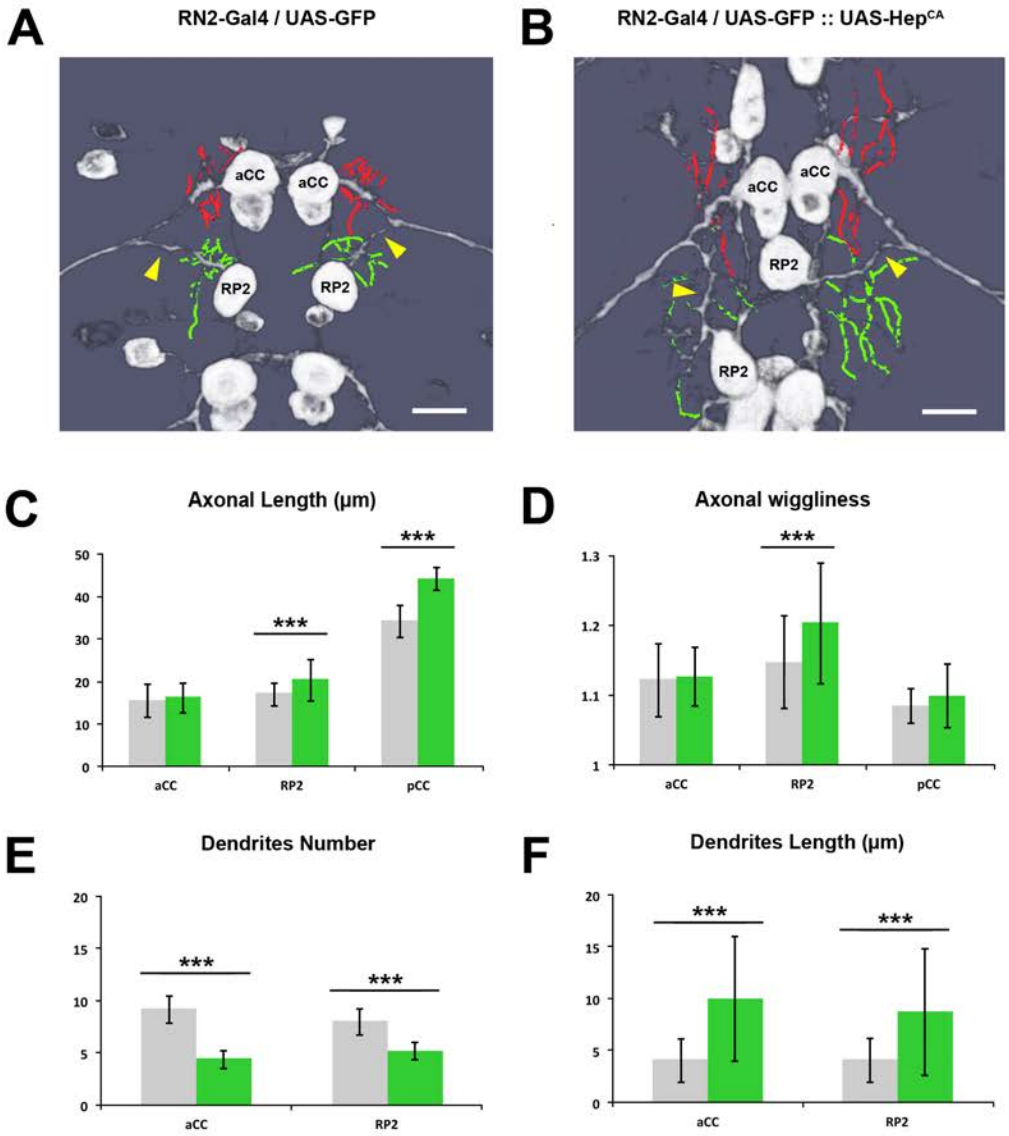
A
RN2-Gal4 / UAS-GFP
aCC
aCC
RP2
RP2
B
RN2-Gal4 / UAS-GFP :: UAS-Hep^CA
aCC
aCC
RP2
RP2
C
Axonal Length (µm)
***
***
aCC
RP2
pCC
D
Axonal wiggliness
***
aCC
RP2
pCC
E
Dendrites Number
***
***
aCC
RP2
F
Dendrites Length (µm)
***
***
aCC
RP2

917

918 **Figure 5. The axonal and dendritic landscape of pioneer neurons is altered upon JNK**
919 **hyperactivation**

920 **A** and **B**) Flat-prepped, stage 16 embryos expressing mCD8-GFP (**A**) and mCD8-GFP and Hep^{CA}
921 (**B**) under the control of the RN2-Gal4 line immunostained for GFP. Traces of the aCC (red) and
922 RP2 (green) proximal dendrites are over-imposed. Yellow arrowheads point to differences in RP2
923 axon morphology. Anterior is up. Scale bar is 10 µm.

924 **C**) Histograms showing the average axonal length of the aCC, RP2 and pCC neurons. Statistically
925 significant differences ($p<0.001$) in the axonal length of the RP2 and pCC neurons were detected
926 between control and Hep^{CA} expressing neurons (n= 4 embryos). Control embryos are represented
927 in grey and Hep^{CA} expressing embryos in green.

928 **D**) Histograms showing the average axonal wiggliness of the aCC, RP2 and pCC neurons. RP2
929 axonal wiggliness was found significantly increased after Hep^{CA} expression ($p<0.001$, n= 4
930 embryos).

931 **E** and **F**) Graphs representing the average Dendrite Number (**E**) and average Dendrite Length (**F**)
932 of the aCC and RP2 neurons. In all cases significant differences were scored in the comparison of
933 control and Hep^{CA} expressing embryos ($p<0.001$, n= 4 embryos).

Figure 6

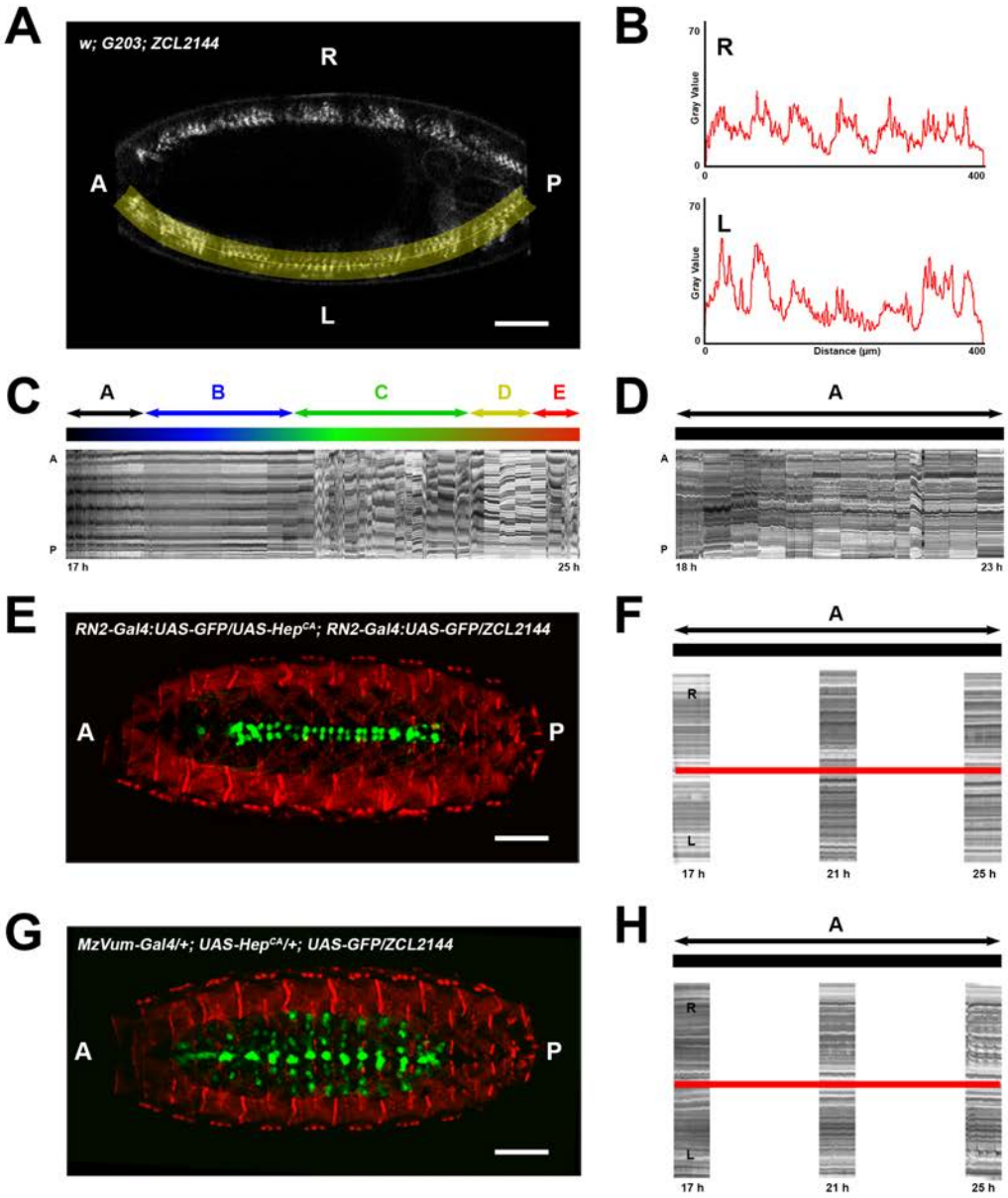
A
w; G203; ZCL2144
R
A
P
L
B
R
70
Gray Value
0
400
L
70
Gray Value
0
Distance (µm)
400
C
A
B
C
D
E
A
P
17 h
25 h
D
A
A
P
18 h
23 h
E
RN2-Gal4:UAS-GFP/UAS-Hep^{CA}; RN2-Gal4:UAS-GFP/ZCL2144
A
P
F
A
R
L
17 h
21 h
25 h
G
MzVum-Gal4/+; UAS-Hep^{CA}/+; UAS-GFP/ZCL2144
A
P
H
A
R
L
17 h
21 h
25 h

934

935 **Figure 6. Defective motor coordination results in incomplete peristalsis in *puc^{E69}* embryos**

936 **A)** Representative mid-plane image of a stage 17 embryo carrying two GFP protein traps expressed
937 at muscle Z-lines (*w; G203; ZCL2144*) (see **Movie S7**). A selected segmented-line (highlighted in
938 yellow) was employed to create kymographs spanning muscle units along the A/P axis (see below)
939 at both sides of the embryo, right (R) and left (L). The evolution overtime of these kymographs
940 was monitored live. Scale bar is 25 µm.

941 **B)** Intensity Profile plots generated along the segmented-line selection in **A**. Gray values as a
942 function of distance highlight the distribution of the segmental muscle units along the axis. Muscle
943 contraction is detected by the differences in the distance between consecutive peaks at sequential
944 time points.

945 **C)** Kymograph displaying muscle profiles from 17 to 25 hours AEL for the left side of the embryo
946 in **A**. Anterior (A) and posterior (P). Motor coordination maturation occurs in 5 stages of
947 approximated stereotyped length (color coded): A, Intense unilateral twitching; B, general
948 inactivity with occasional uncoordinated contractions; C, initiation of backward and forward
949 peristalsis; D, pre-hatching inactivity period and E, complete peristalsis and specialized hatching
950 head movements.

951 **D)** Kymograph displaying muscle profiles from 18 to 23 hours AEL, when the embryo dies, for
952 the left side of a *puc^{E69}* embryo (see **Movie S8**). Anterior (A) and posterior (P). Motor coordination
953 fails and embryos do not progress beyond the unilateral contraction period (stage A).

954 **E** and **G)** Ventral view of stage 17 embryos expressing GFP under the control of the RN2-Gal4
955 (**E**) and MzVum-Gal4 (**G**) lines co-expressing Hep^{CA} and carrying the muscle Z-lines specific GFP
956 protein trap ZCL2144. Muscles are pseudo-colored in red and neurons in green. Scale bar is 25
957 µm.

958 **F** and **H**) Kymographs (ZCL2144 marker) revealing occasional unilateral contractions in embryos
959 co-expressing Hep^{CA} in the RN2-Gal4 (**F**) and MzVum-Gal4 (**H**) neurons. For each case, the
960 kymographs correspond to three periods of 1 hour. These embryos never manage to coordinate
961 muscle movements. Both sides, right (R) and left (L) are shown.

Figure 7

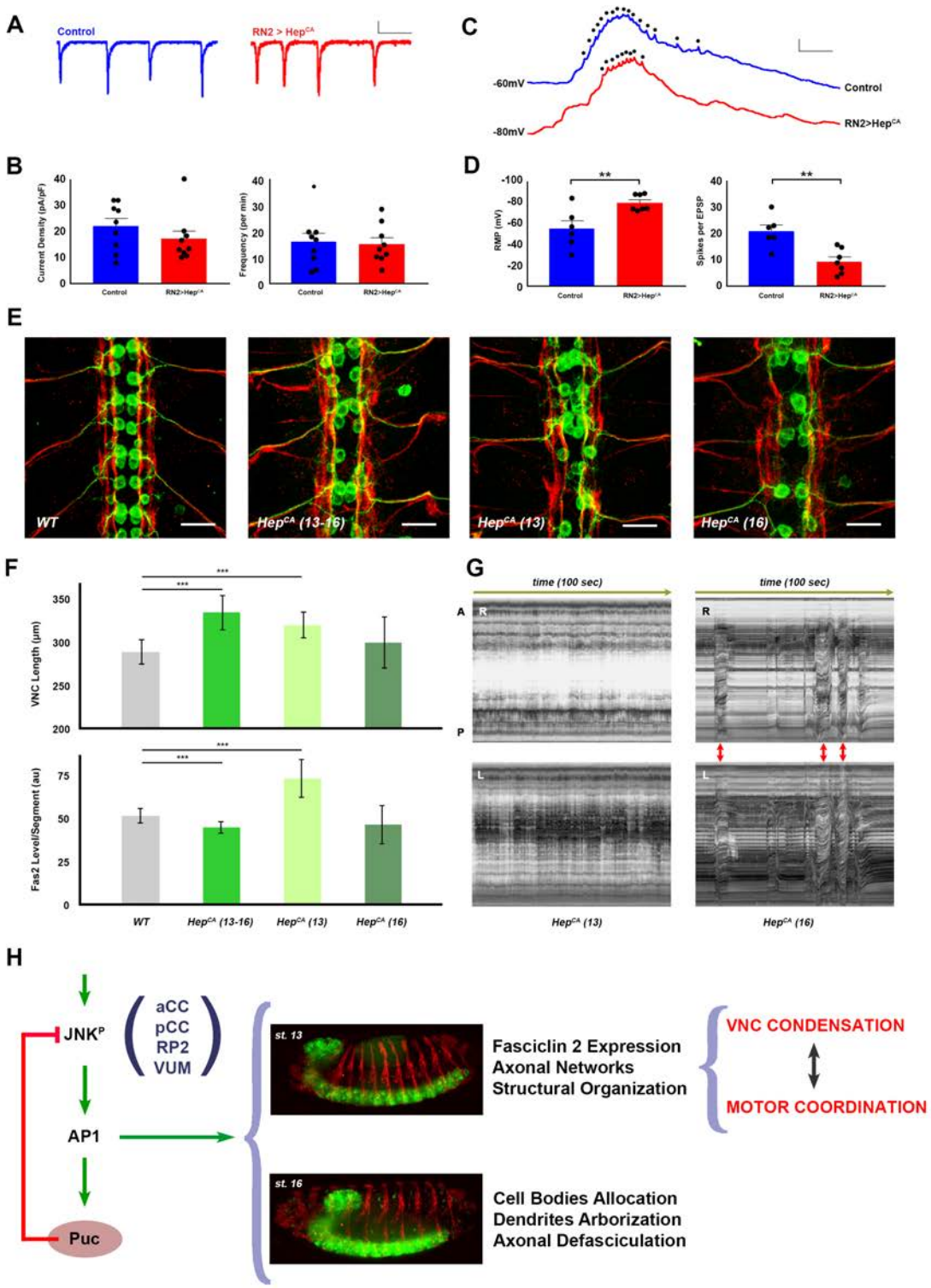
A
Control
RN2 > Hep^CA
C
-60mV
-80mV
Control
RN2>Hep^CA
B
Current Density (pA/pF)
Frequency (per min)
Control
RN2>Hep^CA
D
RMP (mV)
Spikes per EPSP
**
**
E
WT
Hep^CA (13-16)
Hep^CA (13)
Hep^CA (16)
F
VNC Length (µm)
Fas2 Level/Segment (au)
***
WT
Hep^CA (13-16)
Hep^CA (13)
Hep^CA (16)
G
time (100 sec)
A
P
R
L
Hep^CA (13)
Hep^CA (16)
H
JNK^P
AP1
Puc
aCC
pCC
RP2
VUM
st. 13
st. 16
Fasciclin 2 Expression
Axonal Networks
Structural Organization
Cell Bodies Allocation
Dendrites Arborization
Axonal Defasciculation
VNC CONDENSATION
MOTOR COORDINATION

962

963 **Figure 7. JNK activity modulates VNC condensation, neuronal firing and embryo motor**
964 **coordination**

965 **A)** Representative traces of endogenously produced cholinergic SRCs from aCC/RP2
966 motoneurons in late stage 17 embryos in control (*RN2-Gal4 / CyO*) and experimental lines (*RN2-*
967 *Gal4 > UAS-Hep*^{CA}). Scale Bar: 20 pA / 2s.

968 **B)** No significant difference in SRC amplitude (21.7 ± 3.0 vs. 17.0 ± 3.1 pA / pF, control vs. *RN2-*
969 *Gal4 > UAS-Hep*^{CA} respectively, P = 0.28) or frequency (16.3 ± 3.3 vs. 15.4 ± 2.4 per min, P =
970 0.83) was observed.

971 **C)** Representative traces of endogenously produced cholinergic EPSPs from aCC/RP2
972 motoneurons in late stage 17 embryos in control (*RN2-Gal4 / CyO*) and experimental lines (*RN2-*
973 *Gal4 > UAS-Hep*^{CA}). Action potentials are indicated by asterisks. The amplitude of the action
974 potentials is shunted because of the underlying depolarization. Scale Bar: 10 mV / 100ms.

975 **D)** Motoneuron resting membrane potential (RMP) is significantly hyperpolarized in *RN2-Gal4 >*
976 *UAS-Hep*^{CA} (-57.0 ± 7.6 vs. -81.5 ± 2.9 mV, control vs. *RN2-Gal4 > UAS-Hep*^{CA} respectively, P
977 = 0.009). Consequently, the average number of action potentials fired per EPSP was also
978 significantly reduced (20.6 ± 2.4 vs. 9.3 ± 1.7 spikes per EPSP, P = 0.003). All data points are
979 shown on graphs, bars represent mean ± sem.

980 **E)** Fas 2 (red) and GFP (green) immunoreactivity of RN2-Gal4 embryos at late stage 16 subjected
981 to different temperature shift conditions and expressing, from left to right: GFP alone (WT)
982 (maintained at 29ºC continuously from stage 10 to 16); or GFP in combination with a *Hep*^{CA}
983 transgene; Hep^{CA} (10-16) (maintained at 29ºC continuously from stage 10 to 16); Hep^{CA} (10-13)
984 (kept at 29ºC between stages 10 and 13) and Hep^{CA} (15-16) (kept at 29ºC during stages 15 and
985 16). Maximum projection of ventral views across three VNC abdominal segments. Scale Bar is 10
986 µm. Overexpressing *Hep*^{CA} at early stages affects pioneer functions and provoke the collapse of
987 neurons cell bodies into the midline. At late stages, dendrite arborizations, axons fasciculation and
988 cell bodies alignment are disturbed.

989 **F)** Quantification of the VNC length in µm (average and standard deviation) for each condition
990 (**E**) (top). Statistically significant differences in length ($p < 0.0001$) were detected between WT
991 and (Hep^{CA} 10-16) and (Hep^{CA} 10-13) embryos. Quantification of the Average Integrated Density
992 of Fas 2 signal by segment (bottom). Statistically significant differences in Fas 2 levels (p <

993 0.0001) were detected between WT and (Hep^{CA} 10-16) and (Hep^{CA} 10-13) embryos. Note the
994 increased expression of Fas 2 in (Hep^{CA} 10-13) (see Discussion).

995 **G)** Kymographs (bright field) displaying muscle profiles at 25 hours AEL (100 sec) for the left
996 (L) and right (R) sides of embryos expressing Hep^{CA} in RN2+ cells at early (10-13) or late (15-16)
997 developmental stages. Anterior (A) and posterior (P). Embryos overexpressing *Hep^{CA}* at early
998 stages in RN2+ neurons never managed to coordinate muscle movements but those overexpressing
999 *Hep^{CA}* late, developed bilaterally symmetrical peristalsis (red arrows) and hatched in all occasions
1000 (**Movie S10**).

1001 **H)** Regulatory network modulating VNC architectural robustness and condensation and
1002 coordinating motor activities. Precise JNK activity levels in early-specified neurons (aCC, pCC,
1003 RP2 and VUMs) are regulated by a negative feedback loop mediated by Puc. Excessive JNK
1004 activity in *puc* mutants or upon early overexpression of Hep^{CA} in aCC, pCC, RP2 and/or VUMs
1005 neurons leads to a general downregulation of Fas 2 expression (autonomous and non-autonomous),
1006 defects in axonal paths and a general affectation of the architectural robustness of the VNC,
1007 preventing its condensation. The coordination of embryonic motor activities and peristaltic
1008 movements is also inhibited, which could be in part consequence of a failure in wiring optimization
1009 arising from the VNC incomplete condensation. Late interference in JNK activity prevents cell
1010 bodies allocation, dendrites correct arborization and axonal late defasciculation. Images show an
1011 otherwise WT embryo at stages 13 and 16 carrying ELAV-GFP [pan-neural expression (green)]
1012 and Hh-RFP [posterior compartment cells (red)] transgenes.

1013 **SUPPLEMENTAL FIGURES**

Figure S1

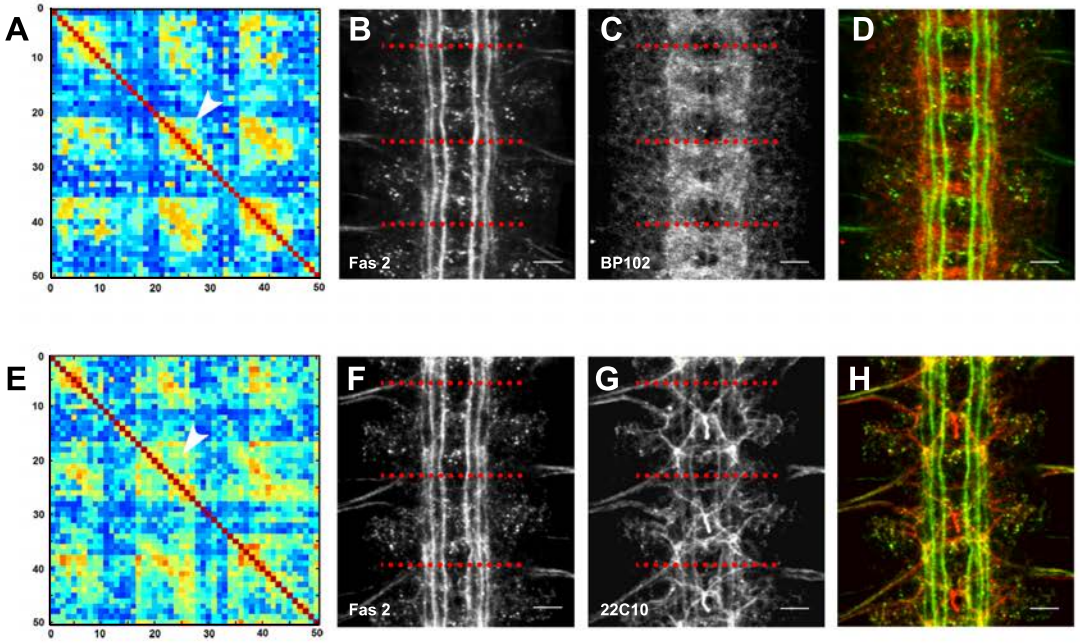

1014

1015 **Figure S1. Fine localization of robustness nodes**

1016 **A)** Self cross-correlation matrix of the Z sections of the image in **B**. A conspicuous node of robust
1017 correlation is highlighted (white arrowhead).

1018 **B** to **D)** Images for Fas 2 (**B** - green in **D**), BP102 (**C** - red in **D**) and their superimposed image (**D**)
1019 of a double-stained 16 stage *wt* embryo. Discontinued red lines indicate the localization of the
1020 robustness nodes in relation to the VNC pattern. Scale Bar is 10 μm.

1021 **E)** Self cross-correlation matrix of the Z sections of the image in **F**. A conspicuous node of robust
1022 correlation is highlighted (white arrowhead).

1023 **F** to **H)** Images for Fas 2 (**F** - green in **H**), 22C10 (**G** - red in **H**) and their superimposed image **(H)**
1024 of a double-stained 16 stage *wt* embryo. Discontinued red lines indicate the localization of the
1025 robustness nodes in relation to the VNC pattern. Scale Bar is 10 μm.

Figure S2

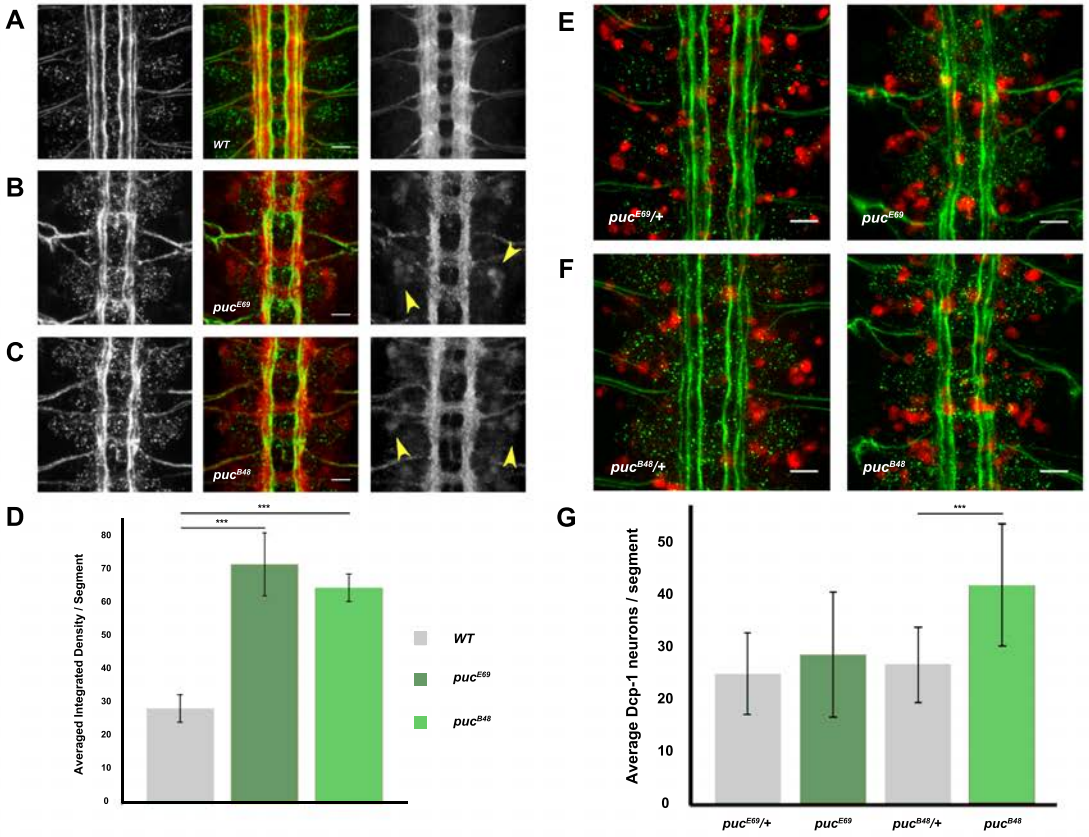

1026

1027 **Figure S2. JNK activity and cell death in *puc* mutants**

1028 **A)** Single (left and right) and combined (center) channels highlighting the expression of Fas 2 (left
1029 - green) and anti-P-JNK (right- red) of a stage 17 *wt* embryo. Scale Bar is 10 µm.

1030 **B)** Equivalent as A for a stage 17 puc^{E69} embryo. Scale Bar is 10 µm.

1031 **C)** Equivalent as A for a stage 17 puc^{B48} embryo. Scale Bar is 10 µm.

1032 In mutant embryos (**B** and **C**) a significant fraction of the P-JNK signal remained in or around cell
1033 bodies (yellow arrowheads) and is not found just in axons as in *wt*.

1034 **D)** Graph displaying the averaged Integrated Density per segment for the P-JNK signal.
1035 Statistically significant differences in P-JNK levels ($p < 0.001$) were detected between the *wt* and
1036 both mutant conditions.

1037 **E)** From left to right, stage 17 heterozygous and homozygous puc^{E69} embryo stained for Fas 2
1038 (green) and Dcp1 (red), which highlights those cells in the process of apoptosis. Scale Bar is 10
1039 µm.

1040 **F)** From left to right, equivalent images as in **E** for the puc^{B48} allele. Scale Bar is 10 µm.

1041 **G)** Graph displaying the averaged Integrated Density per segment for the Dpc1 signal. Statistically
1042 significant differences in Dcp1 levels ($p < 0.001$) were detected between *wt* and puc^{B48} embryos.
1043 The Dpc1 levels of puc^{E69} embryos showed a tendency to be consistently larger than in the *wt*,
1044 although they were not statistically significant.

Figure S3

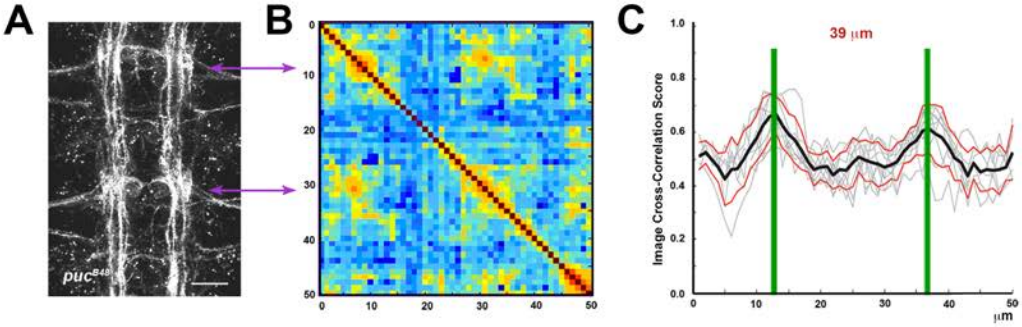

1045

1046 **Figure S3. Robustness and modularity of the VNC architecture in *puc^{B48}* embryos**

1047 **A)** Maximum projection of the VNC of a *Drosophila* 16-stage *puc^{B48}* embryo stained with Fas 2.
1048 Defasciculation and collapse of longitudinal connectives is widely spread. Scale Bar is 10 µm.

1049 **B)** Self cross-correlation matrix of **A**. In *puc^{B48}*, single nodes per segment are consistently
1050 developed (purple double headed arrows).

1051 **C)** Image cross-correlation score along the AP axis for **B** (n=7). Segmental Fas 2 nodes are on
1052 average at 39 µm from each other in *puc^{B48}* and the internodal profile flattens. The grey lines show
1053 individual profiles. The black line corresponds to the Average values and the red lines to the
1054 Standard Deviations. The green bars indicate the positions of maximum correlation (nodes).

Figure S4

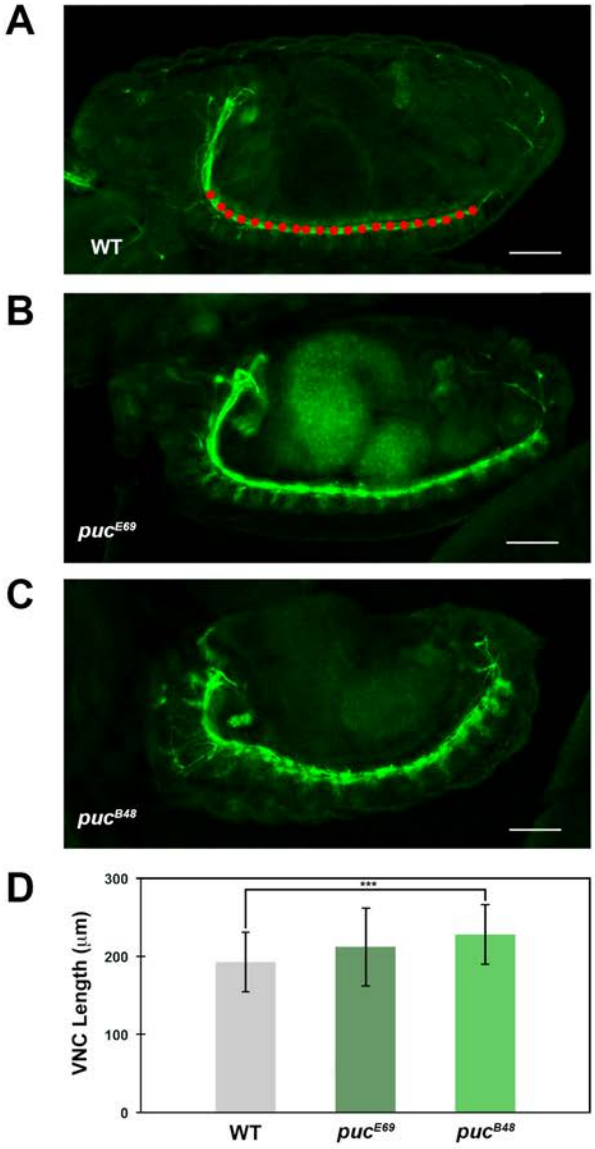

1055

1056 **Figure S4. Loss of VNC condensation in *puc* mutants**

1057 **A)** *wt*, **B)** puc^{E69} and **C)** puc^{B48} embryos Fas 2 immunoreactivity. Lateral view of whole mounts of
1058 stage 17 embryos. Direct measurements of the VNC length were performed along the outline of
1059 the abdominal segments of the VNC as shown in A (dotted red line). Scale Bar is 10 μm.

1060 **D)** Quantification of the VNC length in μm (average and standard deviation) for each condition.
1061 Statistically significant differences in length ($p < 0.001$) were detected between the *wt* and puc^{B48}
1062 embryos. The length of the VNC of puc^{E69} embryos showed a tendency to be consistently longer
1063 than the *wt*, although it was not statistically significant.

Figure S5

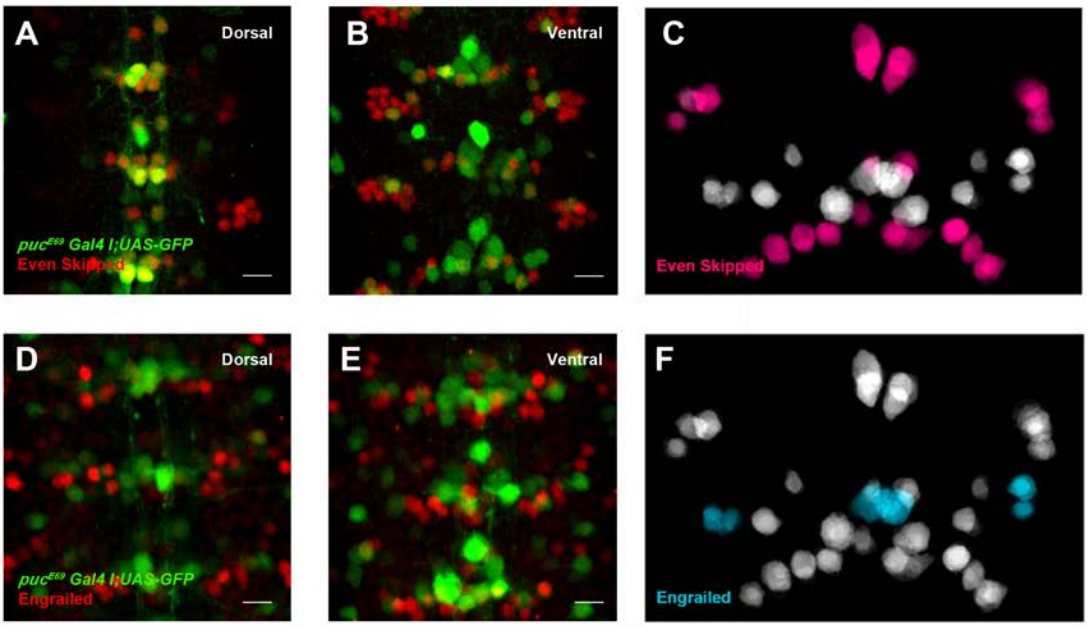

1064

1065 **Figure S5. Identities of *puc*-expressing neurons**

1066 **A** and **B)** Dorsal and ventral sections highlighting the expression of *puc* (green) in the VNC of
1067 stage 17 *puc*^{E69}*I-Gal4* > *UAS-GFP* embryo double-stained for Even-Skipped (red). Scale Bar is
1068 10 µm.

1069 **C)** Diagram indicating those *puc* expressing cells also expressing Even-Skipped [magenta - aCC,
1070 pCC, RP2, U1-U3 (plus weak/variable expression in U4-U5) and 3 out of the 8 to 10 EL
1071 interneurons].

1072 **D** and **E)** Dorsal and ventral sections highlighting the expression of *puc* (green) in the VNC of
1073 stage 17 *puc*^{E69}*I-Gal4* > *UAS-GFP* embryo double-stained for Engrailed (red). Scale Bar is 10 µm.

1074 **F)** Diagram indicating those *puc*-expressing cells also expressing Engrailed (cyan - NL1, NL2,
1075 and iVUM5 neurons).

Figure S6

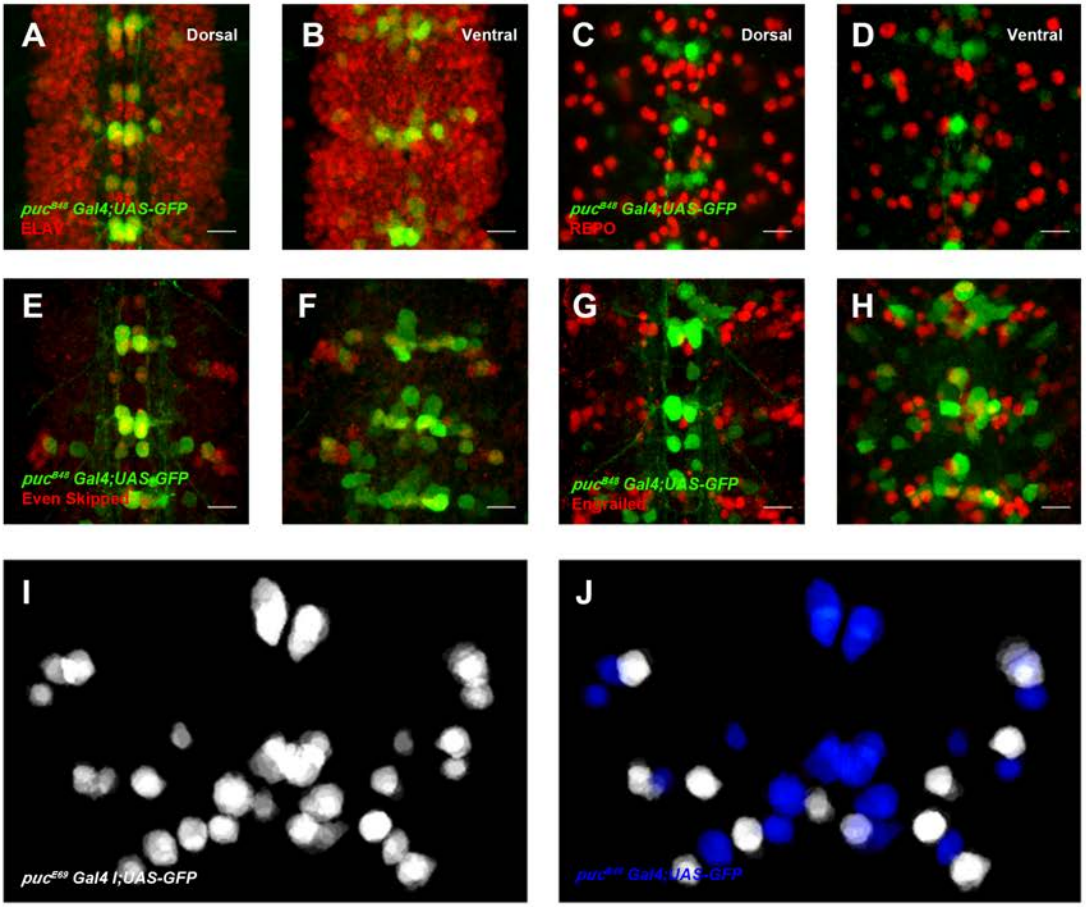

1076

1077 **Figure S6. *puc^{B48}* expressing neurons**

1078 **A** to **D)** Dorsal and ventral sections highlighting the expression of *puc* (green) in the VNC of stage
1079 17 *puc^{B48}-Gal4 > UAS-GFP* embryo double-stained for the pan-neuronal marker Elav (**A** and **B** -
1080 red) or the glial marker Repo (**C** and **D** - red). *puc* is expressed in a subset of neurons in each
1081 segment but not in glia. Scale Bar is 10 µm.

1082 **E** to **H)** Dorsal and ventral sections highlighting the expression of *puc* (green) in the VNC of stage
1083 17 *puc^{B48}-Gal4 > UAS-GFP* embryo double-stained for Even-Skipped (**E** and **F** - red) or Engrailed
1084 (**G** and **H** - red). Scale Bar is 10 µm.

1085 **I)** Cartoon representing the full set of *puc^{B48}* expressing neurons per segment in the VNC.

1086 **J)** Cartoon representing the *puc^{E69}* neurons highlighting the cells expressing *puc^{B48}* (deep blue).

Figure S7

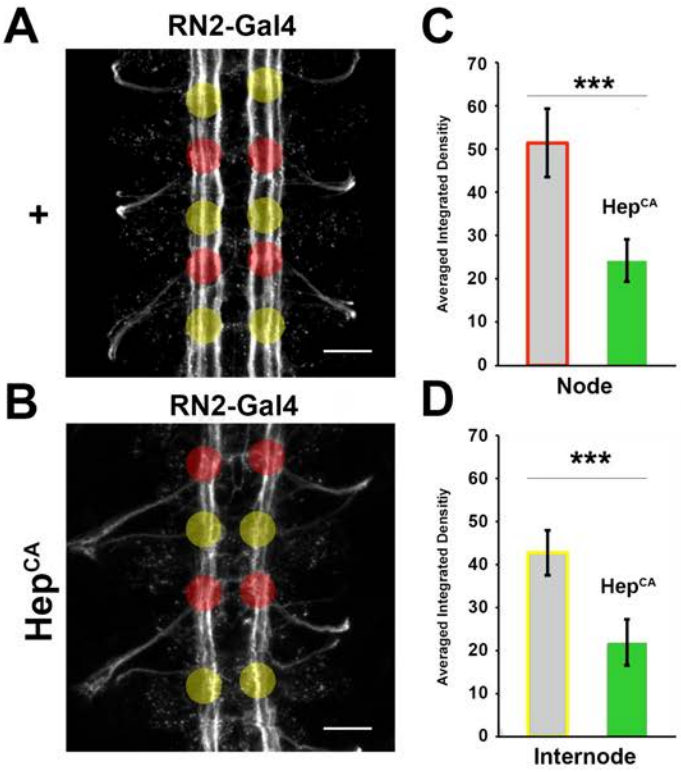

1087

1088 **Figure S7. Fasciclin 2 expression under the control of Hep^{CA}**

1089 **A)** *RN2-Gal4* and **B)** *RN2-Gal4 > UAS-Hep^{CA}* stage 16 embryos Fas 2 immunoreactivity.
1090 Maximum projection of ventral views across two-three VNC abdominal segments. Overlaid circles
1091 represent the fixed area ROIs used for measuring the Average Integrated Density of Fas 2 signal,
1092 either at the node (red) or at the internode (yellow) positions. Scale Bar is 10 µm.

1093 **C** and **D)** Quantification of the Average Integrated Density of Fas 2 signal at node (**C**) and
1094 internode (**D**) positions as indicated. Statistically significant differences in Fas 2 levels ($p < 0.001$)
1095 were detected between embryos expressing and non-expressing Hep^{CA}, both at the node and
1096 internode positions.

Figure S8

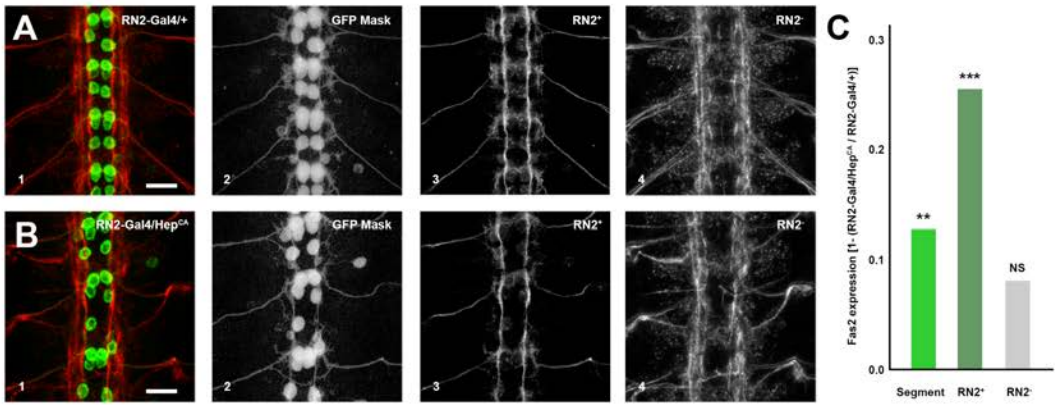

1097

1098 **Figure S8. JNK signaling modulates Fasciclin 2 expression**

1099 **A)** *RN2-Gal4 / +* and **B)** *RN2-Gal4 > UAS-Hep^{CA}* stage 16 embryos Fas 2 immunoreactivity. Sum
1100 projection of ventral views across two-three VNC abdominal segments. Panels from left to right
1101 display: 1) Maximum projection of GFP (RN2-Gal4) (green) and Fas 2 (red) expression; 2) Sum
1102 projection of GFP binary masks; 3) Fas 2 expression associated to RN2^{+} cells; and 4) Fas 2
1103 expression associated to RN2^{-} cells. Scale Bar is 10 µm. **C)** Graphic representation of the reduction
1104 of Fas 2 Average Integrated Density per segment between conditions **B** (HepCA overexpressing
1105 embryos; n=13) and **A** (WT controls; n=6). Statistically significant differences in Fas 2 levels were
1106 detected for whole segments (0.13; $p< 0.01$) and for RN2+ cells (0.25; $P<0.001$) but not for RN2-
1107 cells (0.07; $P>0.05$). JNK hyperactivation in RN2+ cells leads to the autonomous reduction of Fas
1108 2 expression by 25%.

Figure S9

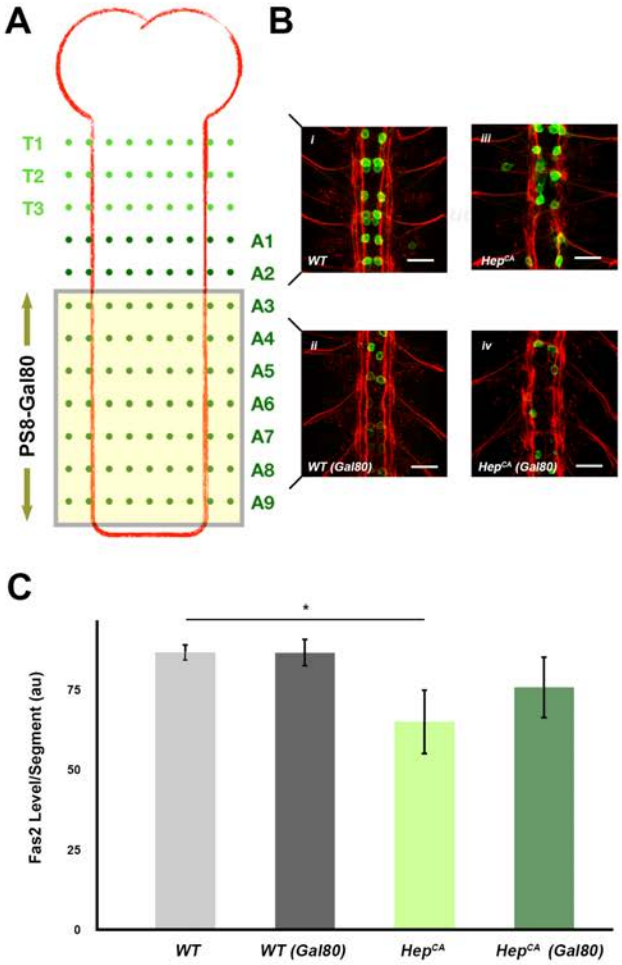

1109

1110 **Figure S9. JNK signaling autonomously modulates Fasciclin 2 expression**

1111 **A)** Cartoon showing a schematic view of the embryonic CNS highlighting the territory of
1112 expression of a Gal80 transgene (PS8-Gal80) under the control of the *iab3* promoter (parasegments
1113 8 to 13) (pale yellow box). Thoracic (pale green) and abdominal (dark green) segments are
1114 indicated. **B)** Maximum projection of ventral views across three VNC segments of *RN2-Gal4 >*
1115 *UAS-GFP* (i and ii) and *RN2-Gal4 > UAS-GFP; UAS-Hep*^{CA} (iii and iv) carrying PS8-Gal80. GFP
1116 expression is shown in green and Fas 2 in red. GFP is highly expressed in RN2 cells in the thoracic
1117 and anterior abdominal segments (i and iii), while its expression is strongly reduced in the posterior
1118 abdominal segments (ii and iv). Scale Bar is 10 μm. **C)** Quantification of the Average Integrated
1119 Density of Fas 2 signal per segment. Statistically significant differences in Fas 2 levels ($p < 0.01$)
1120 were detected between embryos expressing and non-expressing Hep^{CA}, only in areas anterior to
1121 the parasegment 8. Restricting JNK hyperactivation to discrete segments confirm that Fas 2
1122 expression was autonomously regulated by JNK.

Figure S10

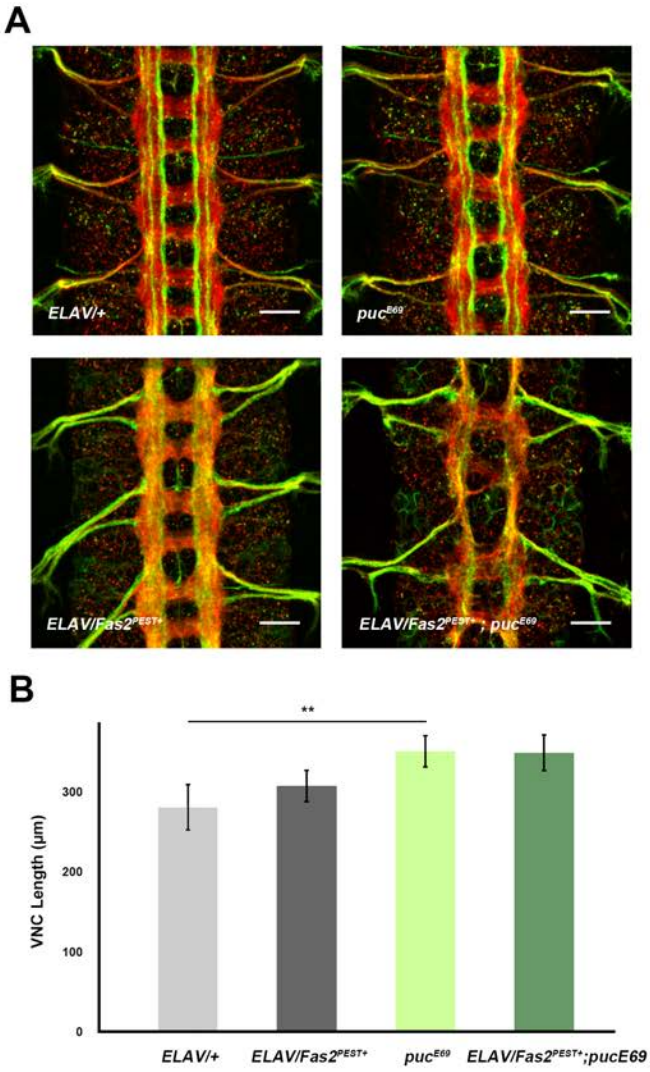

1123

1124 **Figure S10. Fasciclin 2 does not rescue Hep^{CA} overexpression phenotypes**

1125 **A)** Superimposed images for Fas 2 (green) and HRP-TRITC (red) of double-stained 16 stage
1126 *ELAV/+, puc^{E69}, ELAV-Gal4 > UAS-Fas 2^{PEST+},* and *ELAV-Gal4 > UAS-Fas 2^{PEST+}; puc^{E69}*
1127 embryos. Neural expression of Fas 2^{PEST+} in a *puc^{E69}* background exacerbates axonal network
1128 defects. Scale Bar is 10 μm. **B)** Quantification of the VNC length in μm (average and standard
1129 deviation) for each condition. Statistically significant differences in length ($p < 0.001$) were
1130 detected between *wt* and *puc^{E69}* embryos regardless of the presence of Fas 2^{PEST+}. Pan-neural
1131 overexpression of the full length Fas 2^{PEST+} isoform fails to suppress VNC structural or
1132 condensation defects.

Figure S11

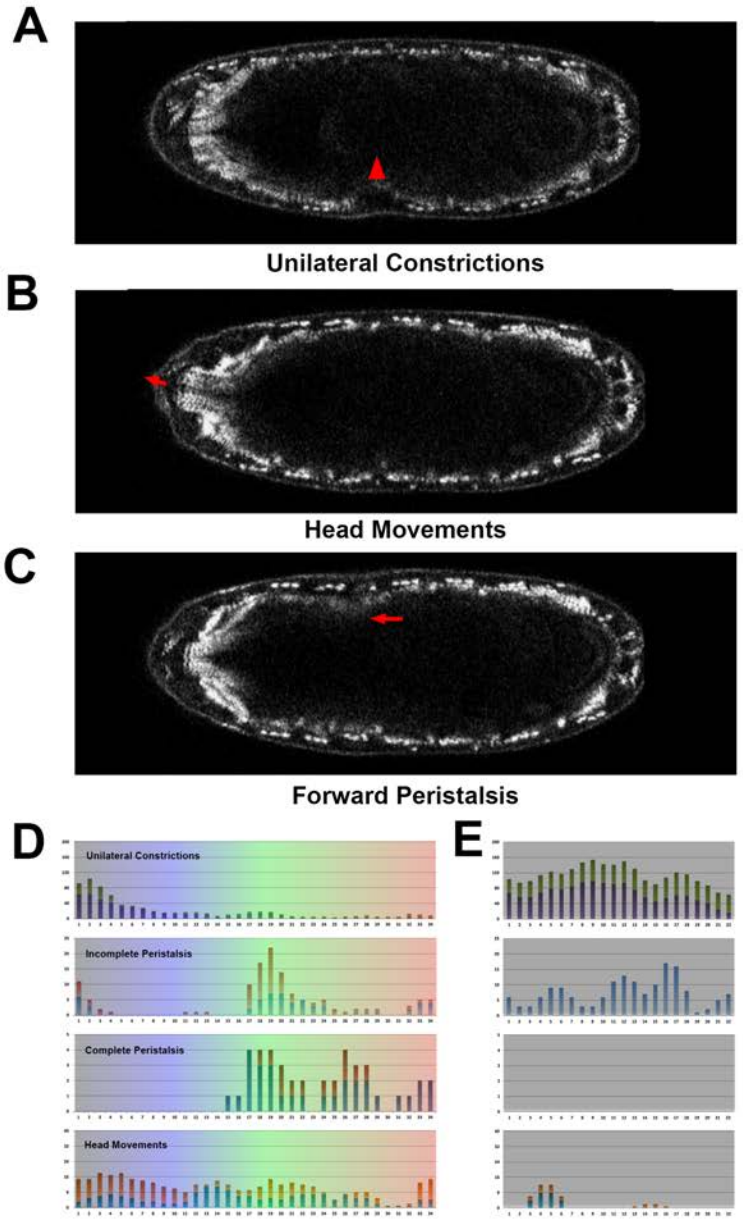

1133

1134 **Figure S11. Types of embryonic muscle movements**

1135 Snapshots from **Movie S6** displaying mid-plane images of a stage 17 embryo carrying two GFP
1136 protein traps expressed at muscle Z-lines (*w; G203, ZCL2144*). Three main types of movement
1137 were observed during the muscle coordination process. Red arrows point to the contracting muscle
1138 units. Anterior is to the left. Scale bar is 50 µm.

1139 **A)** Unilateral muscle contractions. They can occur at any embryo side and in different segments.

1140 **B)** Head turning and mouth hook pinching.

1141 **C)** Peristalsis. They can be incomplete or complete and develop forward (in the image) or
1142 backward displacements.

1143 **D)** Histograms showing the progression of the muscle coordination process in wild type embryos.
1144 Over-imposed colors follow the 5 stages of motor coordination maturation described in **C**. Muscle
1145 movements were distributed in four classes: Unilateral contractions [sum of the contractions
1146 occurring at the right (green) and the left (purple) side of the embryo]; Incomplete peristalsis [sum
1147 of the incomplete forward (blue) and incomplete backward (red) peristaltic attempts]; Complete
1148 peristalsis [sum of the full forward (blue) and backward (red) peristalsis]; and Head movements
1149 [sum of head turning (red) and mouth hook pinching events (blue)].

1150 **E)** Histograms equivalent to **D** showing the unsuccessful muscle coordination of puc^{E69} embryos.

Figure S12

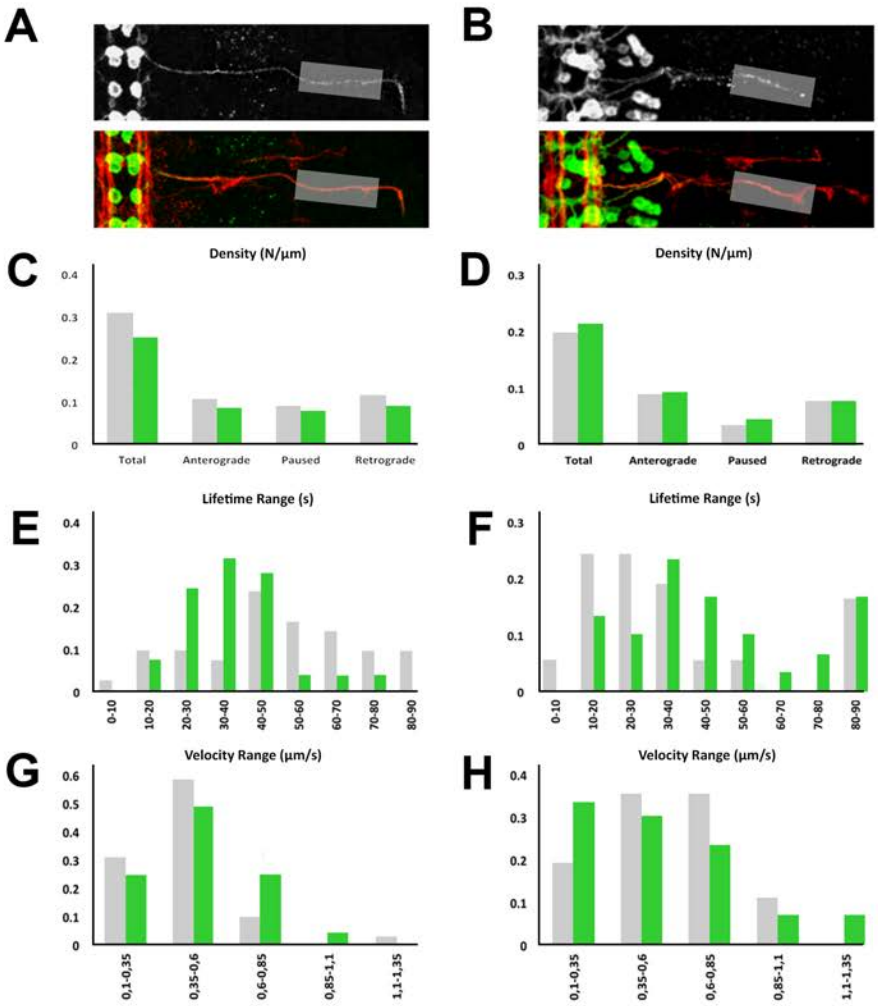

1151

1152 **Figure S12. JNK activity does not affect synaptic vesicle transport**

1153 **A** and **B**) Flat-prepped, stage 16 embryos expressing Synaptotagmin-GFP under the control of the
1154 RN2-Gal4 (**A**) and MzVum-Gal4 (**B**) lines immunostained for GFP (gray scale - top panels and
1155 green - bottom panels) and Fas 2 (red - bottom panel). The grey rectangle marks the medial part
1156 of the ISN, where synaptic vesicles axonal transport was monitored (see **Movie S9**). Scale bar is
1157 25 µm.

1158 **C** and **D**) Histograms showing synaptotagmin vesicles density and directional motility in control
1159 (grey) versus Hep^{CA} expressing (green) aCC/ RP2 (**C**) and VUM motoneurons (**D**). No statistically
1160 significant differences were observed between control and JNK over-active neurons.

1161 **E** and **F**) Lifetime range distribution of motile synaptotagmin vesicles in aCC/RP2 (**E**) and VUM
1162 (**F**) motoneurons. No differences were observed in lifetime between control (grey) and Hep^{CA}
1163 expressing (green) embryos.

1164 **G** and **H**) Mean velocity range distribution comparison of motile synaptotagmin vesicles in
1165 aCC/RP2 (**G**) and VUM (**H**) motoneurons between control (grey) and JNK gain-of function
1166 (green) conditions. For both sets of motoneurons the distribution was unaltered.

1167

1168

1169 **SUPPLEMENTAL MOVIES LEGENDS**

1170

1171 **Movie S1. Fas 2 positive connectives**

1172 Animated 3D reconstruction of the Fas 2 positive connectives of a section of the VNC of a late
1173 embryo (Stage 17).

1174

1175 **Movie S2. Fas 2 positive connectives of a *puc*^{E69} embryo**

1176 Animated 3D reconstruction of the Fas 2 positive connectives of a section of the VNC of a late
1177 *puc*^{E69} mutant embryo (Stage 17).

1178

1179 **Movie S3. Dynamics of *puc*^{E69} expression**

1180 Time course of *puc*^{E69} expression from a *puc*^{E69}*I-Gal4 > UAS-GFP* viable line. *puc* expression can
1181 be observed from early stage 13 in a few neurons at the midline. As development progressed, more
1182 and more neurons express *puc*, both within the VNC and at the peripheral nervous system (PNS).
1183 Scale bar is 50 µm. Anterior is to the left.
1184

1185 **Movie S4. Minimum consensus for the segmental *puc*^{E69} expression**

1186 Animated 3D cartoon representing a single segment of a late *puc*^{E69} mutant embryo (Stage 17).
1187 The 19 *puc* expressing cells per hemisegment represented in the minimum consensus are shown
1188 in different colors.
1189

1190 **Movie S5. Axonal and dendritic landscape of pioneer neurons upon JNK hyper-activation**

1191 Animated 3D reconstruction of the axonal and dendritic pattern of stage 16 embryos expressing
1192 mCD8-GFP (**A**) and mCD8-GFP and Hep^{CA} (**B**) under the control of the RN2-Gal4 line. Traces
1193 of the dendrites (purple) are over-imposed. Scale bar is 10 µm.
1194

1195 **Movie S6. Embryonic motor patterns**

1196 Representative mid-plane movies of a stage 17 embryo carrying two GFP protein traps expressed
1197 at muscle Z-lines (*w; G203; ZCL2144*). **A)** Forward peristalsis. **B)** Backward Peristalsis. **C)** Left
1198 twitch. **D)** Right twitch. **E)** Head tumble. **F)** Mandible pinch. Scale bar is 50 µm. Anterior is to the
1199 left.
1200

1201 **Movie S7. Time course of motor maturation**

1202 Representative mid-plane movies (250 time points per stage) of an embryo carrying two GFP
1203 protein traps expressed at muscle Z-lines (*w; G203; ZCL2144*). From top to bottom stages **A**
1204 (Unilateral twitches and incomplete peristalsis), **B** (Resting period), **C** (Complete peristalsis), **D**
1205 (Late resting period) and **E** (Hatching movements). Color coded as in **Figure 6**. Scale bar is 50
1206 µm. Anterior is to the left.
1207

1208 **Movie S8. Motor activity of *puc*^{E69} embryos**

1209 Representative mid-plane movie (1000 time points) of a late stage 17 *puc*^{E69} embryo carrying two
1210 GFP protein traps expressed at muscle Z-lines (*w; G203; ZCL2144*). Scale bar is 50 µm. Anterior
1211 is to the left.

1212

1213 **Movie S9. Synaptic vesicles axonal transport in RN2 neurons**

1214 Stage 16 embryos expressing Synaptotagmin-GFP under the control of the RN2-Gal4 in the
1215 absence **(A)** or presence **(B)** of Hep^{CA}. Left panels present representative single plane movies (Fire
1216 Luts) with 1 sec interval for a total of 60 cycles. Right panels display in different colors the traces
1217 of the different particles analyzed. Proximal is to the left. Scale bar is 25 µm.

1218

1219 **Movie S10. Motor coordination responses to early and late JNK hyperactivation**

1220 Representative mid-plane movies of stage 17 embryos expressing Hep^{CA} in RN2+ cells at early
1221 (13 - top) or late (16 - bottom) developmental stages. Embryos over-expressing Hep^{CA} at early
1222 stages never coordinate muscle movements but those overexpressing Hep^{CA} late, developed
1223 multiple bilaterally symmetrical peristalsis and hatched. Scale bar is 50 µm

1224